bioRxiv preprint doi: https://doi.org/10.1101/260711; this version posted February 5, 2018. The copyright holder for this preprint (which was not certified by peer review) is the author/funder. All rights reserved. No reuse allowed without permission.

Increased autophagy in ephrinB2 deficient osteocytes is associated with hypermineralized, brittle bones

Christina Vrahnas[1,2], Toby A Dite[2,3], Niloufar Ansari[1,2], Blessing Crimeen-Irwin[1], Huynh Nguyen[4], Mark R Forwood[4], Yifang Hu[5], Mika Ikegame[6], Keith R Bambery[7], Cyril Petibois[8], Mark J Tobin[7], Gordon K Smyth[5,9], Jonathan S Oakhill[2,3,10], T John Martin[1,2] & Natalie A Sims[1,2,11]*

[1]Bone Biology and Disease Unit, St. Vincent's Institute of Medical Research, Melbourne, Victoria, 3065, Australia

[2]Department of Medicine, The University of Melbourne, St. Vincent's Hospital, Melbourne, Victoria, 3065, Australia

[3]Metabolic Signalling Laboratory, St. Vincent's Institute of Medical Research, Melbourne, Victoria, 3065, Australia

[4]School of Medical Science and Menzies Health Institute Queensland, Griffith University, Gold Coast, 4222, Queensland, Australia

[5]Bioinformatics Division, The Walter and Eliza Hall Institute of Medical Research, Parkville, Victoria, 3010, Australia

[6]Department of Oral Morphology, Graduate School of Medicine, Dentistry and Pharmaceutical Sciences, Okayama University, Okayama, 700-8525, Japan

[7]Infrared Microspectroscopy (IRM) Beamline, Australian Synchrotron, Clayton, Victoria, 3168, Australia

[8]University of Bordeaux, Inserm U1029 LAMC, Allée Geoffroy Saint-Hilaire Bat. B2, F33600, Pessac, France

[9]School of Mathematics and Statistics, The University of Melbourne, Melbourne, Victoria, 3010, Australia

[10]Mary MacKillop Institute for Health Research, Australian Catholic University, Victoria, 3065, Australia

[11]Lead contact

Keywords: Osteocytes, PTH, mineralisation, FTIR, autophagy

***Correspondence:** nsims@svi.edu.au

bioRxiv preprint doi: https://doi.org/10.1101/260711; this version posted February 5, 2018. The copyright holder for this preprint (which was not certified by peer review) is the author/funder. All rights reserved. No reuse allowed without permission.

Summary

Mineralized bone forms when collagen-containing osteoid accrues hydroxyapatite crystals. This process has two phases: a rapid initiation (primary mineralization), followed by slower accrual of mineral (secondary mineralization) that continues until that portion of bone is renewed by remodelling. Within the bone matrix is an interconnected network of cells termed osteocytes. These cells are derived from bone-forming osteoblasts. This cellular transition requires expression of ephrinB2, and we were intrigued about why ephrinB2 continues to be expressed at high levels in mature osteocytes. To determine its function in osteocytes, we developed an osteocyte-specific ephrinB2 null mouse and found they exhibited a brittle bone phenotype. This was not caused by a change in bone mass, but by an intrinsic defect in the strength of the bone material. Although the initiation of osteoid mineralization occurred at a normal rate, the process of secondary mineralization was accelerated in these mice. The maturing mineralized bone matrix incorporated mineral and carbonate more rapidly than controls, indicating that osteocytic ephrinB2 suppresses mineral accumulation in bone. No known regulators of mineralization were modified in the bone of these mice. However, RNA sequencing showed differential expression of a group of autophagy-associated genes, and increased autophagic flux was confirmed in ephrinB2 knockdown osteocytes. This indicates that the process of secondary mineralization in bone makes use of autophagic machinery in a manner that is limited by ephrinB2 in osteocytes, and that this process may be disrupted in conditions of bone fragility.

bioRxiv preprint doi: https://doi.org/10.1101/260711; this version posted February 5, 2018. The copyright holder for this preprint (which was not certified by peer review) is the author/funder. All rights reserved. No reuse allowed without permission.

Introduction

The skeleton is unique in the human body because its organic structure is hardened by integration of mineral, allowing it to provide support for locomotion and protection for internal organs. Mineralized bone forms when collagen-containing osteoid, deposited by osteoblasts, accrues hydroxyapatite crystals. The process has two phases: a rapid initiation (primary mineralization), followed by slower accrual of mineral (secondary mineralization) that continues until that portion of bone is renewed by remodeling. During the process, osteoblasts become incorporated in the non-mineralized osteoid and differentiate into osteocytes to form a highly connected network of specialized cells residing within the mineralized matrix[1,2]. In response to stimuli such as mechanical load, hormones, and cytokines, osteocytes release proteins that both stimulate[3] and inhibit[4] the activity of bone forming osteoblasts. Both osteoblasts and osteocytes express proteins that initiate mineralization of the osteoid matrix [4-7], but it is not known how these cells govern the speed of continuing mineral accrual.

Two related agents that stimulate bone formation are the agonists of the parathyroid hormone (PTH) receptor (PTHR1): PTH, and PTH-related protein (PTHrP). Locally-derived PTHrP, from osteoblasts and osteocytes stimulates bone formation in a paracrine manner [8,9], and this action has been exploited by the pharmacological agents teriparatide and abaloparatide. These are the only

bioRxiv preprint doi: https://doi.org/10.1101/260711; this version posted February 5, 2018. The copyright holder for this preprint (which was not certified by peer review) is the author/funder. All rights reserved. No reuse allowed without permission.

pharmacological agents that are currently available clinically that can increase bone mass in patients with fragility fractures [10,11]. Both PTH and PTHrP treatment substantially increase the expression of the contact-dependent signalling molecule ephrinB2 in osteoblasts *in vitro* and in bone *in vivo* [12]. We have previously shown that the interaction of ephrinB2 (gene name: *Efnb2*) with its receptor, EphB4, provides a checkpoint through which osteoblasts must pass to reach late stages of osteoblast and osteocyte differentiation [13-16]. Furthermore, osteoblast-specific deletion of ephrinB2 compromised bone strength by impairing osteoblast differentiation, and delaying the initiation of bone mineralization, ultimately leading to a mild osteomalacia (high osteoid content)[14]. This suggested that primary osteoid mineralization is initiated by osteoblasts after the ephrinB2:EphB4 differentiation checkpoint.

We were intrigued that ephrinB2 expression remains high in fully embedded osteocytes[12], beyond the ephrinB2:EphB4 differentiation checkpoint. Given the extensively connected nature of osteocytes and the contact-dependent nature of ephrinB2:EphB4 signalling, we hypothesized that ephrinB2 regulates the function of osteocytes embedded in the bone matrix. We undertook the present work to determine the requirement for ephrinB2 expression in osteocytes. This revealed that ephrinB2 in osteocytes does not regulate the initiation of mineralization but is required to limit secondary mineral accrual and retain the flexibility of the bone matrix. We also show that, in the absence of ephrinB2, osteocytes exhibit modified

bioRxiv preprint doi: https://doi.org/10.1101/260711; this version posted February 5, 2018. The copyright holder for this preprint (which was not certified by peer review) is the author/funder. All rights reserved. No reuse allowed without permission.

levels of genes associated with autophagy and increased autophagic flux, providing evidence that this process in osteocytes directly controls mineralization.

Results

EphrinB2 is upregulated by PTH and PTHrP in Ocy454 cells.

Upregulation of ephrinB2 expression in osteocytes by PTH and PTHrP stimulation was confirmed in Ocy454 cells (Fig. 1A); PTH(1-34) and PTHrP(1-141) both significantly increased *Efnb2* mRNA levels. shRNA knockdown of PTHrP (*Pthlh*) in Ocy454 cells resulted in significantly lower *Efnb2* mRNA levels at all time points, compared to vector control (Fig. 1B), indicating that endogenous PTHrP expression by osteocytes is required for normal *Efnb2* expression in osteocytes.

Deletion of ephrinB2 in osteocytes results in a brittle bone phenotype

FACS purification of DMP1-GFP+ osteocytes and use of primers targeted to the exon 1-2 boundary of *Efnb2* confirmed the presence of *Efnb2* mRNA in osteocytes of control mice, and effective targeting of *Efnb2* in osteocytes from *Dmp1Cre.Efnb2*$^{f/f}$ mice, while retaining *Efnb2* in non-osteocytic cells (Fig. 1C).

Three-point bending tests demonstrated a strength defect in female *Dmp1Cre.Efnb2*$^{f/f}$ femora compared to *Dmp1Cre.Efnb2*$^{w/w}$ controls (Fig. 2A-F, Table 1). There was no significant difference in bone strength observed in males (data not shown). A significantly higher percentage of bones from *Dmp1Cre.Efnb2*$^{f/f}$ mice

bioRxiv preprint doi: https://doi.org/10.1101/260711; this version posted February 5, 2018. The copyright holder for this preprint (which was not certified by peer review) is the author/funder. All rights reserved. No reuse allowed without permission.

fractured at lower deformation than controls (Fig. 2B). Average load-deformation curves also showed this (Fig. 2A) and indicated that femora from *Dmp1Cre.Efnb2*$^{f/f}$ mice could withstand less force before yielding (Table 1) and before breaking (ultimate force, Fig. 2C), and deformed less at the maximum force that bones could withstand, compared to controls (Fig. 2D). The reduction in ultimate deformation was largely due to a deficit in the extent of deformation from the yield point onwards (Fig. 2E, Table 1). Energy absorbed to failure was also significantly lower in *Dmp1Cre.Efnb2*$^{f/f}$ mice compared to controls (Fig. 2F). Stiffness (the slope of the load / deformation curve before the yield point) was not significantly modified (Table 1). Instead, *Dmp1Cre.Efnb2*$^{f/f}$ femora had a lower yield point, and once they began to yield, they withstood less force and deformed less than controls.

The *Dmp1Cre.Efnb2*$^{f/f}$ mice did not exhibit any significant difference in moment of inertia (Fig. 3A), or dimensions of the cortical bone (Table 1). Consistent with this, when normalized for cortical dimensions, femora from *Dmp1Cre.Efnb2*$^{f/f}$ mice showed impaired material strength compared to controls (Fig. 3B), including lower yield stress and strain (Table 1), lower ultimate stress (Fig. 3C), lower ultimate strain (Fig. 3D), and lower toughness (Fig. 3E); elastic modulus was not significantly altered (Table 1), consistent with the normal stiffness data obtained. Reference point indentation also indicated a change in material strength independent of geometry, with a significantly greater indentation distance increase (IDI) (the increase in the test probe's indentation distance in the last cycle relative to the first cycle) in *Dmp1Cre.Efnb2*$^{f/f}$ bones compared to controls (Fig. 3F). No other parameters measured by RPI were significantly altered (data not shown).

bioRxiv preprint doi: https://doi.org/10.1101/260711; this version posted February 5, 2018. The copyright holder for this preprint (which was not certified by peer review) is the author/funder. All rights reserved. No reuse allowed without permission.

Neither bone mineral density nor bone formation rate are changed in Dmp1Cre.Efnb2$^{f/f}$ bones

Although moment of inertia was unchanged, microCT revealed a slightly lower cortical thickness in *Dmp1Cre.Efnb2$^{f/f}$* femora compared to controls; however, this occurred with no significant lowering of periosteal perimeter, nor any significant change in marrow area (Fig 4A-C). In contrast to *OsxCre.Efnb2$^{f/f}$* mice in which their bone strength phenotype was associated with reduced mineral appositional rate at the periosteum [14], *Dmp1Cre.Efnb2$^{f/f}$* mice exhibited no significant change in periosteal mineral appositional rate (Fig. 4D) or periosteal mineralizing surface (Fig. 4E). *Dmp1Cre.Efnb2$^{f/f}$* femora also showed no significant alteration in cortical tissue mineral density (Fig. 4F).

Bone formation rate was also normal in trabecular bone of *Dmp1Cre.Efnb2$^{f/f}$* bones. Trabecular mineral appositional rate, mineralizing surface and bone formation rate were unchanged between the genotypes (Table 2). There were also no differences detected in osteoid thickness, osteoid surface, osteoblast surface or osteoclast surface in *Dmp1Cre.Efnb2$^{f/f}$* bones compared to controls (Table 2). There was no difference in the proportion of woven to lamellar cortical bone, detected by polarized light microscopy (Table 3).

Backscattered electron microscopy detected no change in osteocyte lacunar size or the top 20% largest lacunae in the femoral midshaft of *Dmp1Cre.Efnb2$^{f/f}$* mice,

bioRxiv preprint doi: https://doi.org/10.1101/260711; this version posted February 5, 2018. The copyright holder for this preprint (which was not certified by peer review) is the author/funder. All rights reserved. No reuse allowed without permission.

however osteocyte lacunar density was significantly greater compared to controls (Table 3), suggesting an alteration in the rate of osteocyte incorporation into the bone matrix during bone formation and/or mineralisation.

Dmp1Cre.Efnb2$^{f/f}$ mice have greater mineral and carbonate deposition

Since the brittle bone phenotype in *Dmp1Cre.Efnb2$^{f/f}$* mice was not explained by any changes detected by microCT or histomorphometry, and since the (blinded) technician cutting the sections for histomorphometry noted that some samples were very difficult to cut, we used sFTIRM to measure bone composition. Measurements were made at the periosteum, a region lacking bone remodelling, thereby allowing assessment of the bone matrix as mineralization[17]. Three regions of increasing matrix maturity were measured (Fig. 5A). Average spectra for each genotype, taken from the intermediate region indicated altered spectral geometry in *Dmp1Cre.Efnb2$^{f/f}$* bone compared to controls (Fig. 5B). They had higher phosphate and carbonate peaks indicating a greater level of mineralization. In addition, *Dmp1Cre.Efnb2$^{f/f}$* bone showed a lower amide I peak, but higher amide II peak, suggesting greater compaction of collagen in *Dmp1Cre.Efnb2$^{f/f}$* mice.

When quantified, control bones showed the changes associated with bone matrix maturation that we have previously reported on murine periosteum and rabbit Haversian bone: with increasing depth from the bone edge, mineral:matrix and carbonate:mineral ratios increase, while amide I:II ratio decreases [17] (Fig. 5C-E). Collagen crosslinking, which represents the post-translational modification of

bioRxiv preprint doi: https://doi.org/10.1101/260711; this version posted February 5, 2018. The copyright holder for this preprint (which was not certified by peer review) is the author/funder. All rights reserved. No reuse allowed without permission.

collagen that provides tensile strength and viscoelasticity of collagen fibers [18], did not change in control bones with increasing bone maturity (Fig. 5F). The process of mineral accrual was accelerated in *Dmp1Cre.Efnb2*$^{f/f}$ bone (Fig. 5C,D): in the two most immature regions of bone on the periosteum, mineral:matrix ratio was significantly greater in *Dmp1Cre.Efnb2*$^{f/f}$ bone compared to control (Fig. 5C) and conversely, amide I:II ratio was significantly lower (Fig. 5E). In addition, although carbonate:mineral ratio did not increase significantly in the three regions measured in the control mice, there was a significant increase in carbonate:mineral ratio with increasing matrix maturity in the *Dmp1Cre.Efnb2*$^{f/f}$ bone (Fig. 5E). Mature *Dmp1Cre.Efnb2*$^{f/f}$ bone reached a higher level of carbonate:mineral ratio than controls in the two more mature regions. The increase in mineral:matrix ratio was purely due to an increase in mineral content and not lower collagen content levels, shown by significantly greater levels of hydroxyproline, a major component of collagen (Table 3). Collagen crosslinking was significantly greater in the intermediate region of *Dmp1Cre.Efnb2*$^{f/f}$ bones (Fig. 5F) indicating that crosslinks mature in the same region in which mineral and carbonate accumulate. Since greater collagen crosslinks have previously been observed in osteoporotic patients [18], this also suggests that the more mature bone in *Dmp1Cre.Efnb2*$^{f/f}$ mice is related to the brittle bone phenotype.

Since the amide I:II ratio has not yet been validated in bone as an indicator of collagen orientation, we used polarized light FTIR imaging (pFTIRI) to visualize and quantitate the spatial variation of collagen fibers in the same region assessed by

bioRxiv preprint doi: https://doi.org/10.1101/260711; this version posted February 5, 2018. The copyright holder for this preprint (which was not certified by peer review) is the author/funder. All rights reserved. No reuse allowed without permission.

sFTIRM. The 0° and 90° polarizing filter was used to magnify the signal from molecular bonds oriented parallel and perpendicular orientation, respectively, to the bone tissue section surface [19]. The pFTIRI 0° polarizing filter result validated the sFTIRM observations: a significantly lower amide I:II ratio was observed on the periosteal edge in *Dmp1Cre.Efnb2*$^{f/f}$ bones compared to control (Fig. 6C). In control tibiae, pFTIRI with a 0° polarizing filter indicated amplified amide I signal on both periosteal and endocortical surfaces while the amide II signal remained even across the cortical bone (Fig. 6A). Quantitation confirmed this, showing a significantly greater amide I:II ratio in both periosteal and endocortical regions compared to the central cortical region (Fig. 6C). In *Dmp1Cre.Efnb2*$^{f/f}$ mice, the difference in amide I:II ratio between periosteal and central cortical regions was no longer detected, and both these regions showed significantly lower amide I:II ratio than the endocortical region (Fig. 6B,C). Quantitation of pFTIRI confirmed the sFTIRM result by showing significantly lower amide I:II ratio on the periosteal surface of *Dmp1Cre.Efnb2*$^{f/f}$ bones compared to controls (Fig. 6C). The amide I signal was amplified to a similar extent by the 90° polarizing filter in control bone (Fig. 6A). In contrast, the amide II signal was greatly amplified on the endocortical edge, compared to levels observed with the 0° polarizing filter (Fig. 6D). The amide I:II ratio was significantly higher in the periosteal region than both the central cortical and endocortical regions in both control and *Dmp1Cre.Efnb2*$^{f/f}$ tibiae (Fig. 6F). The amide II signal in *Dmp1Cre.Efnb2*$^{f/f}$ tibiae was amplified on the endocortical surface (Fig. 6C).

bioRxiv preprint doi: https://doi.org/10.1101/260711; this version posted February 5, 2018. The copyright holder for this preprint (which was not certified by peer review) is the author/funder. All rights reserved. No reuse allowed without permission.

EphrinB2 deficiency in vitro leads to dysregulation of autophagy-related genes, and increased autophagy

To identify mechanisms by which ephrinB2-deficiency alters mineral and matrix composition leading to fragile bones, RNA sequencing was performed on marrow-flushed femora of 12-week old *Dmp1Cre.Efnb2*$^{f/f}$ and control mice. 30 differentially expressed genes were identified; none have previously been associated with osteocyte function, bone mineralisation, or ephrinB2 function (Fig. 7A,B). We noted, and confirmed through a literature search, that ten of these differentially expressed genes are associated with the process of autophagy. Six were upregulated in the ephrinB2-deficient bone: *Fam134b* [20], *Fbxo32* [21,22], *Lama2* [23], *Bnip3* [24,25], *Trim63* [26] and *Peg3* [27]. The other four were downregulated: *Eps8l1*[28], *Klf1* [29] and *Tspo2*[30] and *Unc5a* [31].

To identify whether suppression of ephrinB2 in osteocytes leads to increased autophagy in an independent cell-specific model, we generated stably *Efnb2* deficient Ocy454 osteocytes and assessed autophagy levels. Stable *Efnb2* knockdown was confirmed in mature Ocy454 cells at days 11 and 14 (Fig. 7C). The rate of autophagy was measured by assessing LC3-II:I ratio in *Efnb2* shRNA knockdown cells treated with the autophagic flux inhibitor chloroquine (CQ) [32]. This allows measurement of autophagosome formation. CQ treatment caused a significant elevation in LC3-II:I ratio in both vector and *Efnb2* knockdown cells, as anticipated. This effect was amplified in *Efnb2* shRNA knockdown cells, shown by the increased fold change of CQ-treated *Efnb2* knockdown cells compared to

bioRxiv preprint doi: https://doi.org/10.1101/260711; this version posted February 5, 2018. The copyright holder for this preprint (which was not certified by peer review) is the author/funder. All rights reserved. No reuse allowed without permission.

untreated cells. This indicated that ephrinB2-deficient osteocytes have greater susceptibility to autophagy than vector control (Fig. 7D).

Discussion

This work demonstrates that bone flexibility is maintained, and mineral accrual limited, by ephrinB2 signalling in osteocytes. In the absence of ephrinB2, autophagic processes are increased, and although the initiation of osteoid mineralization occurs at a normal rate, as soon as the process commences, mineral deposition and maturation is accelerated resulting in a brittle bone phenotype. This indicates that the control mechanisms for primary and secondary mineralization are different, and that osteocytes within the bone matrix not only control the initiation of mineralization, but also control its progression. This has major implications for understanding how osteocytes contribute to bone strength.

Bone strength is controlled by both bone mass, and the composition of the bone matrix itself. Bone mass is determined by the balance between the activities of bone forming osteoblasts and bone-resorbing osteoclasts. Bone compositional strength is determined by the content and orientation of collagen, as well as the content and nature of mineral crystals within that collagen network. Previously it has been noted that major defects in bone compositional strength can result from defective collagen deposition (as in osteogenesis imperfecta) or delayed initiation of mineralisation (as in osteomalacia or rickets). In this study, we report a third possible cause of bone fragility: accelerated maturation of the mineralized bone matrix (Figure 8). Hydroxyapatite is comprised of calcium, phosphate and hydroxyl ions which can be

bioRxiv preprint doi: https://doi.org/10.1101/260711; this version posted February 5, 2018. The copyright holder for this preprint (which was not certified by peer review) is the author/funder. All rights reserved. No reuse allowed without permission.

replaced by fluoride, chloride or carbonate. In brittle *Dmp1Cre.Efnb2$^{f/f}$* bones, mineral:matrix ratio in the earliest region of mineral deposition was higher than controls. Since there was no difference in the rate at which osteoid mineralization was initiated (MAR) between these mice and controls, it appears that as soon as mineralization was initiated it commenced rapidly: essentially, mineral was "dumped" into the matrix, reaching mineralization levels of more mature matrix very rapidly. The normal gradual increase in mineral:matrix ratio, previously described in murine, rabbit, rat, baboon and human cortical bone [17,33-37], is accelerated in the absence of ephrinB2. This was not the only aspect of mineral accumulation that was modified. As hydroxyapatite matures in bone, carbonate: mineral ratio increases due to carbonate substitution for phosphate or hydroxyl ions [17,38-41]. *Dmp1Cre.Efnb2$^{f/f}$* bones also showed a more rapid increase in carbonate incorporation within the bone matrix.

A third aspect of bone matrix maturation was accelerated in *Dmp1Cre.Efnb2$^{f/f}$* bones: the reduction in the amide I:II ratio. We have previously reported that the amide I:II ratio declines with increasing mineral accumulation in control mice, likely as a result of more compaction (or steric hindrance) of the collagen molecule in the perpendicular direction as mineral accumulates [17]. The early lowering of the amide I:II ratio in *Dmp1Cre.Efnb2$^{f/f}$* bone indicates a greater rate of collagen compaction as mineral accumulates in the matrix. Amide I:II ratio represents peptide bond vibrations within the collagen molecule [42]. Amide I (C=O stretch) and amide II (C-N, N-H bend) molecular vibrations exhibit dichroism perpendicular (*z*-axis direction)

bioRxiv preprint doi: https://doi.org/10.1101/260711; this version posted February 5, 2018. The copyright holder for this preprint (which was not certified by peer review) is the author/funder. All rights reserved. No reuse allowed without permission.

and parallel (*x*-axis) to the collagen molecular triple helix axis, respectively [43]. This process is exaggerated in *Dmp1Cre.Efnb2*$^{f/f}$ mice. Use of the 0° polarizing filter suggests that increase in collagen compaction is specific to those collagen fibers aligned longitudinally to the bone section. This suggests that these fibers may be more important for absorbing mechanical forces along the length of the tibiae and their altered organization could also contribute to the bone brittleness in ephrinB2-deficient mice.

Another aspect of bone matrix maturation that was accelerated was the incorporation of osteocytes into the bone matrix: *Dmp1Cre.Efnb2*$^{f/f}$ mice exhibited a greater osteocyte density. As osteoid is deposited, a subset of osteoblasts become incorporated into the bone matrix: these are the cells that differentiate into osteocytes. Our data suggests that these pre-osteocytes are incorporated into the bone matrix at a faster rate in *Dmp1Cre.Efnb2*$^{f/f}$ bone. *Dmp1Cre* targets late osteoblasts at the stage where they become embedded within the newly formed bone [44,45], and the greater density of osteocytes that develops may promote mineral accumulation and carbonate incorporation in *Dmp1Cre.Efnb2*$^{f/f}$ bones.

Although this is the first report of a low amide I:II ratio being associated with bone fragility, the cause of the brittle phenotype is likely to be the combination of reduced amide I:II, and increased mineral:matrix and carbonate:mineral. The association of high carbonate with increased bone fragility is consistent with earlier work describing a higher carbonate:mineral ratio in bone specimens from women with

bioRxiv preprint doi: https://doi.org/10.1101/260711; this version posted February 5, 2018. The copyright holder for this preprint (which was not certified by peer review) is the author/funder. All rights reserved. No reuse allowed without permission.

postmenopausal osteoporosis [46] or with greater fracture susceptibility [47]. High mineral:matrix ratio has also been reported in other examples of bone brittleness, such as patients with atypical femoral fracture [48], and murine models of osteogenesis imperfecta, in which it is accompanied by defects in collagen or cartilage content [49,50]. The latter two are both associated with defects in osteoblast function, but the present model exhibited no change in osteoblast function.

A comparison of this mouse model with our earlier mouse that lacked ephrinB2 throughout the osteoblast lineage[14] provides new information about the specific stages of osteoblast/osteocyte differentiation and their roles in the process of bone mineralization. Our earlier model lacking ephrinB2 throughout the osteoblast lineage (*OsxCre.Efnb2*$^{f/f}$) did not exhibit a brittle bone phenotype, but had bones that were more elastic due to delayed initiation of primary mineralization [14]. This indicated that the stage of osteoblast differentiation that controls primary mineralization is beyond the ephrinB2:EphB4 differentiation checkpoint. In *Dmp1Cre.Efnb2*$^{f/f}$ mice, osteoblasts would survive past the checkpoint at which anti-apoptotic action of ephrinB2 is required; this has allowed us to define an action for EphrinB2 later in osteoblast differentiation. Normal initiation of mineralization in *Dmp1Cre.Efnb2*$^{f/f}$ bone indicates that the stage of osteoblast differentiation controlling this process is after the ephrinB2:EphB4 checkpoint, but before the stage of *Dmp1Cre* expression. The stage of osteoblast/osteocyte differentiation after *Dmp1Cre* is expressed does not control initiation of mineralization but controls the rate at which mineral accumulates (Figure 8). Since PTH and PTHrP promote

bioRxiv preprint doi: https://doi.org/10.1101/260711; this version posted February 5, 2018. The copyright holder for this preprint (which was not certified by peer review) is the author/funder. All rights reserved. No reuse allowed without permission.

ephrinB2 expression in both osteoblasts [12]and osteocytes, we suggest that these proteins both promote the initiation of osteoid mineralization and restrain the rate of mineral accrual. While there is no evidence for altered mineral accrual with pharmacological administration of PTH [17], the reduced material strength of mice with PTHrP deletion targeted to osteocytes provides support for a role of PTHrP in regulating mineral accrual via ephrinB2-dependent actions in the osteocyte [9].

The processes that control the rate of mineral accumulation in bone are poorly defined and our data suggests that autophagic processes in the osteocyte that are inhibited by ephrinB2 play a major role to limit this process. Unbiased RNA sequencing identified dysregulation of a range of autophagy-associated genes but detected no changes in mRNA levels of genes known to regulate the initiation of mineralization (*Dmp1* and *Mepe*). We confirmed that ephrinB2 inhibits autophagy *in vitro.* Autophagy is a lysosome-based pathway that contributes to diverse cellular functions, such as adaptation to starvation, quality control of intracellular processes, protein secretion, and elimination of intracellular microbes [51-53]. While explorations of the role of autophagy in osteocytes is in its infancy, previous works have demonstrated that autophagy is increased during osteoblast differentiation [54], and that mice with osteoblast-lineage or osteocytic deletion of either *Atg5* or *Atg7* have reduced autophagy and reduced osteoblast numbers [54-56]. In *Dmp1Cre.Efnb2$^{f/f}$* mice osteoblast numbers were not altered, and we observed no changes in *Atg5* or *Atg7*, suggesting a subset of autophagic processes that control mineral maturation without controlling osteoblast differentiation are modified in the absence of

bioRxiv preprint doi: https://doi.org/10.1101/260711; this version posted February 5, 2018. The copyright holder for this preprint (which was not certified by peer review) is the author/funder. All rights reserved. No reuse allowed without permission.

ephrinB2. None of these regulated genes has a previously known role in osteoblasts or osteocytes.

We suggest there are two possible ways that increased autophagic flux may be associated with the brittle bone phenotype: (1) by controlling osteocyte differentiation and adaptation to the mineralized environment, and (2) by contributing to mineral secretion. As osteocytes become embedded in bone mineral, they develop dendritic extensions and adjust to a more hypoxic environment [57]. Autophagic processes may contribute to this transition by allowing osteocyte to break down complex molecules to use for energy [58], promoting faster organelle recycling, and preservation of nutrients. Mineralization involves the release of cell-derived extracellular membrane-enclosed particles of poorly crystalline mineral, termed matrix vesicles [59,60] and subsequent nucleation (ordered crystal formation) of that amorphous mineral by heterogeneous nucleation driven by contact with collagen, and by secretion of competent apatite nucleators [61-63]. Nollet *et. al* suggested that osteoblasts may use autophagic vacuoles as vehicles for apatite crystal secretion into the extracellular space via exocytotic processes [54]; we propose that osteocytes may also release mineral through this process. Direct release of mineral by osteocytes has been noted both during remineralization of osteocyte lacunae after lactation [64] and in egg-laying hens [65]. Our data suggest that physiological bone formation also requires the secretion of both vesicles and nucleators by osteocytes. We suggest that ephrinB2-deficient osteocytes use

bioRxiv preprint doi: https://doi.org/10.1101/260711; this version posted February 5, 2018. The copyright holder for this preprint (which was not certified by peer review) is the author/funder. All rights reserved. No reuse allowed without permission.

autophagic machinery to release more matrix vesicles and apatite nucleators, thereby driving an increase in bone mineral, resulting in brittle bone matrix.

These findings have implications for other organ systems. EphrinB2 in odontoblasts, which are closely related cells to osteoblasts and osteocytes [66,67] may also control mineralisation in teeth. Pathological mineralisation, such as that in heterotopic ossification after trauma [68], vascular or renal calcification [69,70] may also be modified by ephrinB2 and its influence on autophagic genes, since ephrinB2 is also expressed in those tissues.

In conclusion, ephrinB2 is required to restrain autophagy in the osteocyte, and to prevent the formation of brittle bone. Osteocytic ephrinB2 limits the accumulation of mineral and carbonate substitution within the hydroxyapatite matrix and maintains collagen fiber compaction. This may provide a mechanism by which bone strength is regulated independently of bone size, and independently of osteoblast and osteoclast activities. This provides new information on the mechanisms by which osteocytes control the rate of bone mineralization, and thereby control bone strength.

bioRxiv preprint doi: https://doi.org/10.1101/260711; this version posted February 5, 2018. The copyright holder for this preprint (which was not certified by peer review) is the author/funder. All rights reserved. No reuse allowed without permission.

Experimental Procedures

Cell culture

The osteocytic cell line, Ocy454 cells, were cultured in αMEM supplemented with 10% FBS and 1% Penicillin-Streptomycin-Amphotericin B and Glutamax [71]. Cells were cultured in 2D cell cultures using sex-well plates or in 3D culture using Reinnervate® Alvetex scaffold 6-well inserts (Pittsburgh, PA, USA) and differentiated for up to 14 days as indicated in individual experiments. To study how *Efnb2* mRNA is regulated by PTH and PTHrP, Ocy454 cells were differentiated for 14 days. At day 14 of differentiation, cells were serum starved overnight in αMEM supplemented with 1% FBS and 1% PSA and Glutamax. Cells were then treated with Human PTH(1-34) (10 nM) or Human PTHrP(1-141) (10 nM) for 6 hours. After 6 hours, cells were washed with phosphate buffered saline (PBS) and RNA samples were collected as described below. Additional details of cell culture procedures are described in Supplemental Experimental Procedures.

Pthlh knockdown

shRNA with sequence 5'CCG-GCC-AAT-TAT-TCC-TGT-CAC-TGT-TCT-CGA-GAA-CAG-TGA-CAG-GAA-TAA-TTG-GTT-TTT-TG-3'was used to knock down *Pthlh* in Ocy454 cells [9]. Knockdown was assessed by quantitative real-time PCR (qRT-PCR) at day 0 (undifferentiated), day 7 and day 14 (differentiated) [9]. Additional details of *Pthlh* knockdown procedures are described in Supplemental Experimental Procedures.

bioRxiv preprint doi: https://doi.org/10.1101/260711; this version posted February 5, 2018. The copyright holder for this preprint (which was not certified by peer review) is the author/funder. All rights reserved. No reuse allowed without permission.

qRT-PCR Analysis

RNA was extracted by RNA extraction kits with on-column DNase digestion (Qiagen, Limburg, Netherlands; Bioline, London, UK), or TriSure reagent (Bioline, London, UK). Primers specific to *Efnb2;* forward 5'-GTGCCAGACAAGAGCCATGAA-3' and reverse 5'-GGTGCTAGAACCTGGATTTGG-3' [12]. Gene expression *for Pthlh* knockdown cells was analysed using the Multiplex SensiMix II Probe kits (Bioline, London, UK) with primers specific to *Efnb2*, as previously described [13]. Gene expression levels between samples was normalized to hypoxanthine phospho-ribosyltransferase 1 (*Hprt1*) expression. Relative expression was quantified using the comparative CT method ($2^{-(\text{Gene Ct} - \text{Normalizer Ct})}$). Additional details of qRT-PCR analysis are described in Supplemental Experimental Procedures

Mice

Dmp1Cre mice (Tg(Dmp1-Cre)^{1Jqfe}) (containing the DMP1 10-kb promoter region) were obtained from Lynda Bonewald (University of Kansas, Kansas City, KS, USA) [44] and ephrinB2-floxed (Efnb2^{tm1And}) mice were obtained from David J. Anderson (Howard Hughes Medical Institute, California Institute of Technology, Pasadena, CA, USA) [72]; all mice were backcrossed onto C57BL/6 background. Mice hemizygous for Dmp1Cre were crossed with Efnb2$^{f/f}$ mice to generate Dmp1Cre.Efnb2$^{f/w}$ breeders, which were used to generate ephrinb2 deficient (Dmp1Cre.Efnb2$^{f/f}$) mice and Dmp1Cre.Efnb2$^{w/w}$ littermates or cousins, which were used as controls for all experiments. To generate GFP+ osteocytes, these mice were crossed with Dmp1-GFP (Tg(Dmp1-Topaz)^{1lkal} mice obtained from Dr Ivo Kalajzic, University of Connecticut

bioRxiv preprint doi: https://doi.org/10.1101/260711; this version posted February 5, 2018. The copyright holder for this preprint (which was not certified by peer review) is the author/funder. All rights reserved. No reuse allowed without permission.

Health Science Center, via the colony of Dr Hong Zhou, ANZAC Research Institute, Sydney [73]. For all tissue collections, mice were fasted for 12 hours prior to anesthesia with ketamine and blood was collected via cardiac puncture, as previously described [74]. Both male and female mice were analysed. All animal procedures were conducted with approval from the St. Vincent's Health Melbourne Animal Ethics Committee.

Confirmation of Efnb2 mRNA targeting in osteocytes

To confirm specific targeting of *Efnb2* mRNA in osteocytes, *Dmp1Cre.Efnb2$^{f/f}$* mice were crossed with *Dmp1-GFP* mice to allow purification of osteocytes by fluorescence-activated cell sorting (FACS), according to our previously published methods [9,75]. Osteocytes from 6-week old *Dmp1Cre.Dmp1-GFP-Tg.Efnb2$^{w/w}$* and *Dmp1Cre.Dmp1-GFP-Tg.Efnb2$^{f/f}$* mice were isolated from marrow-flushed long bones and sorted with excitation 488 nm and 530/30 or 530/40-emission filter for GFP on a BD FACS Influx cell sorter (BD Biosciences, Scoresby, Australia). RNA was extracted and *efnB2* mRNA expression was quantified. Additional details of osteocyte purification and qRT-PCR analysis are described in Supplemental Experimental Procedures.

3-point bending and Reference Point Indentation (RPI)

Structural and material properties were analysed in femora from male and female 12-week-old mice by 3-point bending, as described previously [74]. Load-

bioRxiv preprint doi: https://doi.org/10.1101/260711; this version posted February 5, 2018. The copyright holder for this preprint (which was not certified by peer review) is the author/funder. All rights reserved. No reuse allowed without permission.

displacement curves were recorded at a crosshead speed of 1.0 mm/s using an Instron 5564A dual column material testing system, and Bluehill 2 software (Instron, Norwood, MA, USA). Local bone material properties were examined by reference point indentation (RPI) using a BP2 probe assembly apparatus (Biodent Hfc; Active Life Scientific Inc., Santa Barbara, CA, USA), as previously described [74]. Details of 3-point bending tests and RPI procedures are described in Supplemental Experimental Procedures.

Histomorphometry, back scatter electron microscopy (BSEM) and Micro-Computed Tomography (microCT)

Tibiae from 12-week-old female mice were fixed in 4% paraformaldehyde, embedded in methyl methacrylate (MMA), sectioned longitudinally and stained as described previously [13]. Calcein was administered by intraperitoneal (IP) injection 7 and 2 days before tissue collection. Polarized light microscopy and BSEM were performed on 100 μm thick transverse sections from the femoral mid-shaft generated using an Isomet Saw (Buehler, Lake Bluff, IL, USA); measurements included the entire bone interface. BSEM was used to acquire gray-level images of mineralized cortical bone to identify the number of osteocyte lacunae. MicroCT was performed on femora using the SkyScan 1076 system (Bruker-microCT, Kontich, Belgium). Additional details of histomorphometry, BSEM and microCT procedures are described in Supplemental Experimental Procedures.

bioRxiv preprint doi: https://doi.org/10.1101/260711; this version posted February 5, 2018. The copyright holder for this preprint (which was not certified by peer review) is the author/funder. All rights reserved. No reuse allowed without permission.

Synchrotron-based Fourier Transform Infrared Microspectroscopy (sFTIRM) and polarized light FTIR Imaging (pFTIRI)

sFTIRM was used to examine bone composition at the cortical diaphysis in 3μm longitudinal sections of methyl methacrylate (MMA)-embedded tibiae. sFTIRM mapping was performed with the synchrotron source, using a 15 x 15 μm aperture, represented by the 3 regions within the cortex. Spectra were collected from these 3 regions which progressed perpendicularly into the cortex with the first positioned at the periosteal edge (Fig 5A). All data acquisition was undertaken with Bruker OPUS version 6.5 and data analysis completed with OPUS version 7.2. Additional details of sFTIRM and pFTIRI analysis are described in Supplemental Experimental Procedures.

pFTIRI was applied to the same 3μm tibial sections at the same cortical diaphyseal region of analysis used for sFTIRM. This time, larger regions were imaged using a 340 x 340μm aperture either side of the 1500 μm mid-point. All infrared images were obtained in transmission mode. The images were obtained from sub-routines of the Opus 7.5 software (Bruker-Optics, France). To quantitate region specific changes in amide I:II, the diaphyseal cortex was divided into thirds to obtain images of periosteal, intracortical and endocortical regions of interest and quantitated using CytoSpec 1.4.0.3 (Bruker). The FTIR microscope was coupled with two polarizing filters to measure molecular orientation of collagen fibers relative to the plane of the tissue section. The 0° polarizing filter was used to measure bonds "in plane" (parallel to the section). The 90° polarizing filter was used to measure bonds "out of

bioRxiv preprint doi: https://doi.org/10.1101/260711; this version posted February 5, 2018. The copyright holder for this preprint (which was not certified by peer review) is the author/funder. All rights reserved. No reuse allowed without permission.

plane" (perpendicular to the section). This allowed quantification of collagen fibers aligned in different directions through the diaphyseal cortex. Additional details of sFTIRM and pFTIRI analysis are described in Supplemental Experimental Procedures.

Hydroxyproline assay in hydrolyzed bone samples

Following mechanical testing, all fragments of the broken femora were flushed of marrow, hydrolyzed and used for hydroxyproline assay to measure collagen content (31). Absorbance was measured using a POLARstar plate reader at 550nm and interpolated on the standard curve [76]. Additional details of the hydroxyproline assay are described in Supplemental Experimental Procedures.

RNA sequencing

RNA samples were collected from flushed femora of 12-week old female *Dmp1Cre.Efnb2*$^{f/f}$ and cousin-bred control mice. RNA sequencing was conducted on an Illumina HiSeq at the Australian Genome Research Facility to produce 100bp paired-end reads. Reads were mapped to the mouse genome (mm10) using Rsubread [77]. Differential expression between the genotypes was assessed using empirical Bayes moderated t-statistics allowing for an abundance trend in the standard errors and for robust estimation of the Bayesian hyperparameters [78]. The Benjamini and Hochberg method was used to adjust the p-values so as to control the false discovery rate. Differentially expressed genes were analysed based on up-regulated and downregulated and sorted from low to high False Discovery Rate

bioRxiv preprint doi: https://doi.org/10.1101/260711; this version posted February 5, 2018. The copyright holder for this preprint (which was not certified by peer review) is the author/funder. All rights reserved. No reuse allowed without permission.

(FDR). Additional details of RNA Sequencing are described in Supplemental Experimental Procedures.

shRNA knockdown of ephrinB2 in Ocy454 cells

shRNA constructs used to knock down ephrinB2 included shRNA 1 (5' -CGG-GTG-TTA-CAG-TAG-CCT-TAT- 3') and shRNA 2 (5'-CAG-ATT-GTG-TAC-ATA-GAG-CAA-T-3') were obtained from Sigma-Aldrich (St. Louis, MO, USA). These shRNA were cloned into a lentiviral vector PLKO, as previously reported [9] and infected by retrovirus into undifferentiated Ocy454 cells. Infected cells were selected with puromycin (5μg/mL) and cultured at permissive temperature (33°C) before transfer to 37°C for differentiation. Knockdown was validated by quantitative real-time PCR (qRT-PCR), as previously mentioned.

Western blot analysis of chloroquine-treated Ocy454 cells

To test the level of autophagy in osteocytes lacking *Efnb2,* Ocy454 cells with *Efnb2* shRNA knockdown and vector controls were differentiated for 11 days and treated with chloroquine (40μm), a lysosomal degradation inhibitor, for 4 hours. Immunoblots were visualized on an Odyssey membrane imaging system (LI-COR Biosciences) and the LC3II:I ratio was quantitated as the fold change of chloroquine-treated samples relative to basal levels of each construct. Additional details of western blotting are described in Supplemental Experimental Procedures.

bioRxiv preprint doi: https://doi.org/10.1101/260711; this version posted February 5, 2018. The copyright holder for this preprint (which was not certified by peer review) is the author/funder. All rights reserved. No reuse allowed without permission.

Statistics

All graphs show mean ± SEM; number of samples (n) is reported in the figure legends. Statistical significance was determined by unpaired Student's t-tests for histomorphometric, mechanical and microCT analysis, and two-way ANOVA with Fisher's LSD test for sFTIRM-derived data (GraphPad Prism 6 (version 6.05)). $p<0.05$ was considered statistically significant.

bioRxiv preprint doi: https://doi.org/10.1101/260711; this version posted February 5, 2018. The copyright holder for this preprint (which was not certified by peer review) is the author/funder. All rights reserved. No reuse allowed without permission.

References

1 Buenzli, P. R. & Sims, N. A. Quantifying the osteocyte network in the human skeleton. *Bone* **75**, 144-150, doi:10.1016/j.bone.2015.02.016 (2015).

2 Schaffler, M. B., Cheung, W. Y., Majeska, R. & Kennedy, O. Osteocytes: master orchestrators of bone. *Calcified tissue international* **94**, 5-24, doi:10.1007/s00223-013-9790-y (2014).

3 Walker, E. C. *et al.* Oncostatin M promotes bone formation independently of resorption when signaling through leukemia inhibitory factor receptor in mice. *J Clin Invest* **120**, 582-592, doi:10.1172/JCI40568 (2010).

4 Poole, K. E. *et al.* Sclerostin is a delayed secreted product of osteocytes that inhibits bone formation. *FASEB J* **19**, 1842-1844, doi:10.1096/fj.05-4221fje (2005).

5 Houston, B., Stewart, A. J. & Farquharson, C. PHOSPHO1-A novel phosphatase specifically expressed at sites of mineralisation in bone and cartilage. *Bone* **34**, 629-637, doi:10.1016/j.bone.2003.12.023 (2004).

6 Ling, Y. *et al.* DMP1 depletion decreases bone mineralization in vivo: an FTIR imaging analysis. *J Bone Miner Res* **20**, 2169-2177, doi:10.1359/JBMR.050815 (2005).

7 Gowen, L. C. *et al.* Targeted disruption of the osteoblast/osteocyte factor 45 gene (OF45) results in increased bone formation and bone mass. *J Biol Chem* **278**, 1998-2007, doi:10.1074/jbc.M203250200 (2003).

8 Miao, D. *et al.* Osteoblast-derived PTHrP is a potent endogenous bone anabolic agent that modifies the therapeutic efficacy of administered PTH 1-34. *J Clin Invest* **115**, 2402-2411 (2005).

9 Ansari, N. *et al.* Autocrine and Paracrine Regulation of the Murine Skeleton by Osteocyte-Derived Parathyroid Hormone-Related Protein. *J Bone Miner Res*, doi:10.1002/jbmr.3291 (2017).

10 Lindsay, R. *et al.* Effects of a one-month treatment with PTH(1-34) on bone formation on cancellous, endocortical, and periosteal surfaces of the human ilium. *J Bone Miner Res* **22**, 495-502, doi:10.1359/jbmr.070104 (2007).

11 Miller, P. D. *et al.* Effect of Abaloparatide vs Placebo on New Vertebral Fractures in Postmenopausal Women With Osteoporosis: A Randomized Clinical Trial. *JAMA* **316**, 722-733, doi:10.1001/jama.2016.11136 (2016).

12 Allan, E. H. *et al.* EphrinB2 regulation by PTH and PTHrP revealed by molecular profiling in differentiating osteoblasts. *J Bone Miner Res* **23**, 1170-1181, doi:10.1359/jbmr.080324 (2008).

13 Takyar, F. M. *et al.* EphrinB2/EphB4 inhibition in the osteoblast lineage modifies the anabolic response to parathyroid hormone. *J Bone Miner Res* **28**, 912-925, doi:10.1002/jbmr.1820 (2013).

14 Tonna, S. *et al.* EphrinB2 signaling in osteoblasts promotes bone mineralization by preventing apoptosis. *FASEB J* **28**, 4482-4496, doi:10.1096/fj.14-254300 (2014).

bioRxiv preprint doi: https://doi.org/10.1101/260711; this version posted February 5, 2018. The copyright holder for this preprint (which was not certified by peer review) is the author/funder. All rights reserved. No reuse allowed without permission.

15 Sims, N. A. & Vrahnas, C. Regulation of cortical and trabecular bone mass by communication between osteoblasts, osteocytes and osteoclasts. *Arch Biochem Biophys* **561**, 22-28, doi:10.1016/j.abb.2014.05.015 (2014).

16 Martin, T. J. *et al.* Communication between ephrinB2 and EphB4 within the osteoblast lineage. *Advances in experimental medicine and biology* **658**, 51-60, doi:10.1007/978-1-4419-1050-9_6 (2010).

17 Vrahnas, C. *et al.* Anabolic action of parathyroid hormone (PTH) does not compromise bone matrix mineral composition or maturation. *Bone* **93**, 146-154, doi:10.1016/j.bone.2016.09.022 (2016).

18 Paschalis, E. P. *et al.* Bone fragility and collagen cross-links. *J Bone Miner Res* **19**, 2000-2004, doi:10.1359/JBMR.040820 (2004).

19 Bi, X., Li, G., Doty, S. B. & Camacho, N. P. A novel method for determination of collagen orientation in cartilage by Fourier transform infrared imaging spectroscopy (FT-IRIS). *Osteoarthritis and cartilage* **13**, 1050-1058, doi:10.1016/j.joca.2005.07.008 (2005).

20 Khaminets, A. *et al.* Regulation of endoplasmic reticulum turnover by selective autophagy. *Nature* **522**, 354-358, doi:10.1038/nature14498 (2015).

21 Sandri, M. *et al.* Foxo transcription factors induce the atrophy-related ubiquitin ligase atrogin-1 and cause skeletal muscle atrophy. *Cell* **117**, 399-412 (2004).

22 Zaglia, T. *et al.* Atrogin-1 deficiency promotes cardiomyopathy and premature death via impaired autophagy. *J Clin Invest* **124**, 2410-2424, doi:10.1172/JCI66339 (2014).

23 Carmignac, V. *et al.* Autophagy is increased in laminin α2 chain-deficient muscle and its inhibition improves muscle morphology in a mouse model of MDC1A. *Human Molecular Genetics* **20**, 4891-4902, doi:10.1093/hmg/ddr427 (2011).

24 Bellot, G. *et al.* Hypoxia-induced autophagy is mediated through hypoxia-inducible factor induction of BNIP3 and BNIP3L via their BH3 domains. *Molecular and cellular biology* **29**, 2570-2581, doi:10.1128/MCB.00166-09 (2009).

25 Hanna, R. A. *et al.* Microtubule-associated protein 1 light chain 3 (LC3) interacts with Bnip3 protein to selectively remove endoplasmic reticulum and mitochondria via autophagy. *J Biol Chem* **287**, 19094-19104, doi:10.1074/jbc.M111.322933 (2012).

26 Nascimbeni, A. C., Fanin, M., Masiero, E., Angelini, C. & Sandri, M. Impaired autophagy contributes to muscle atrophy in glycogen storage disease type II patients. *Autophagy* **8**, 1697-1700, doi:10.4161/auto.21691 (2012).

27 Buraschi, S. *et al.* Decorin causes autophagy in endothelial cells via Peg3. *Proceedings of the National Academy of Sciences of the United States of America* **110**, E2582-2591, doi:10.1073/pnas.1305732110 (2013).

28 Schoenherr, C. *et al.* Eps8 controls Src- and FAK-dependent phenotypes in squamous carcinoma cells. *J Cell Sci* **127**, 5303-5316, doi:10.1242/jcs.157560 (2014).

bioRxiv preprint doi: https://doi.org/10.1101/260711; this version posted February 5, 2018. The copyright holder for this preprint (which was not certified by peer review) is the author/funder. All rights reserved. No reuse allowed without permission.

29 Magor, G. W. *et al.* KLF1-null neonates display hydrops fetalis and a deranged erythroid transcriptome. *Blood* **125**, 2405-2417, doi:10.1182/blood-2014-08-590968 (2015).

30 Hachez, C. *et al.* The Arabidopsis abiotic stress-induced TSPO-related protein reduces cell-surface expression of the aquaporin PIP2;7 through protein-protein interactions and autophagic degradation. *The Plant cell* **26**, 4974-4990, doi:10.1105/tpc.114.134080 (2014).

31 Plissonnier, M. L. *et al.* Reciprocal antagonism between the netrin-1 receptor uncoordinated-phenotype-5A (UNC5A) and the hepatitis C virus. *Oncogene*, doi:10.1038/onc.2017.271 (2017).

32 Fedorko, M. Effect of chloroquine on morphology of cytoplasmic granules in maturing human leukocytes--an ultrastructural study. *J Clin Invest* **46**, 1932-1942, doi:10.1172/JCI105683 (1967).

33 Fuchs, R. K. *et al.* In situ examination of the time-course for secondary mineralization of Haversian bone using synchrotron Fourier transform infrared microspectroscopy. *Matrix Biol* **27**, 34-41, doi:10.1016/j.matbio.2007.07.006 (2008).

34 Donnelly, E., Boskey, A. L., Baker, S. P. & van der Meulen, M. C. Effects of tissue age on bone tissue material composition and nanomechanical properties in the rat cortex. *Journal of biomedical materials research. Part A* **92**, 1048-1056, doi:10.1002/jbm.a.32442 (2010).

35 Gourion-Arsiquaud, S. *et al.* Spatial variation in osteonal bone properties relative to tissue and animal age. *Journal of bone and mineral research : the official journal of the American Society for Bone and Mineral Research* **24**, 1271-1281, doi:10.1359/jbmr.090201 (2009).

36 Paschalis, E. P. *et al.* FTIR microspectroscopic analysis of human osteonal bone. *Calcified tissue international* **59**, 480-487 (1996).

37 Paschalis, E. P., Betts, F., DiCarlo, E., Mendelsohn, R. & Boskey, A. L. FTIR microspectroscopic analysis of normal human cortical and trabecular bone. *Calcified tissue international* **61**, 480-486 (1997).

38 Rey, C., Renugopalakrishnan, V., Collins, B. & Glimcher, M. J. Fourier transform infrared spectroscopic study of the carbonate ions in bone mineral during aging. *Calcified tissue international* **49**, 251-258 (1991).

39 Legros, R., Balmain, N. & Bonel, G. Age-related changes in mineral of rat and bovine cortical bone. *Calcified tissue international* **41**, 137-144 (1987).

40 Akkus, O., Adar, F. & Schaffler, M. B. Age-related changes in physicochemical properties of mineral crystals are related to impaired mechanical function of cortical bone. *Bone* **34**, 443-453, doi:10.1016/j.bone.2003.11.003 (2004).

41 Rey, C., Collins, B., Goehl, T., Dickson, I. R. & Glimcher, M. J. The carbonate environment in bone mineral: a resolution-enhanced Fourier Transform Infrared Spectroscopy Study. *Calcified tissue international* **45**, 157-164 (1989).

42 Gadaleta, S. J., Landis, W. J., Boskey, A. L. & Mendelsohn, R. Polarized FT-IR microscopy of calcified turkey leg tendon. *Connect Tissue Res* **34**, 203-211 (1996).

bioRxiv preprint doi: https://doi.org/10.1101/260711; this version posted February 5, 2018. The copyright holder for this preprint (which was not certified by peer review) is the author/funder. All rights reserved. No reuse allowed without permission.

43 Fraser, R. & MacRae, T. *Conformation in Fibrous Proteins and Related Synthetic Polypeptides*. (Academic Press, 1973).

44 Lu, Y. *et al.* DMP1-targeted Cre expression in odontoblasts and osteocytes. *Journal of dental research* **86**, 320-325 (2007).

45 Toyosawa, S. *et al.* Dentin matrix protein 1 is predominantly expressed in chicken and rat osteocytes but not in osteoblasts. *J Bone Miner Res* **16**, 2017-2026, doi:10.1359/jbmr.2001.16.11.2017 (2001).

46 Gadeleta, S. J. *et al.* A physical, chemical, and mechanical study of lumbar vertebrae from normal, ovariectomized, and nandrolone decanoate-treated cynomolgus monkeys (Macaca fascicularis). *Bone* **27**, 541-550 (2000).

47 McCreadie, B. R. *et al.* Bone tissue compositional differences in women with and without osteoporotic fracture. *Bone* **39**, 1190-1195, doi:10.1016/j.bone.2006.06.008 (2006).

48 Lloyd, A. A. *et al.* Atypical fracture with long-term bisphosphonate therapy is associated with altered cortical composition and reduced fracture resistance. *Proceedings of the National Academy of Sciences of the United States of America* **114**, 8722-8727, doi:10.1073/pnas.1704460114 (2017).

49 Lietman, C. D. *et al.* A transgenic mouse model of OI type V supports a neomorphic mechanism of the IFITM5 mutation. *J Bone Miner Res* **30**, 489-498, doi:10.1002/jbmr.2363 (2015).

50 Fratzl-Zelman, N. *et al.* Bone matrix hypermineralization in prolyl-3 hydroxylase 1 deficient mice. *Bone* **85**, 15-22, doi:10.1016/j.bone.2016.01.018 (2016).

51 Levine, B. & Kroemer, G. Autophagy in the pathogenesis of disease. *Cell* **132**, 27-42, doi:10.1016/j.cell.2007.12.018 (2008).

52 Mizushima, N. & Komatsu, M. Autophagy: renovation of cells and tissues. *Cell* **147**, 728-741, doi:10.1016/j.cell.2011.10.026 (2011).

53 Ponpuak, M. *et al.* Secretory autophagy. *Curr Opin Cell Biol* **35**, 106-116, doi:10.1016/j.ceb.2015.04.016 (2015).

54 Nollet, M. *et al.* Autophagy in osteoblasts is involved in mineralization and bone homeostasis. *Autophagy* **10**, 1965-1977, doi:10.4161/auto.36182 (2014).

55 Onal, M. *et al.* Suppression of autophagy in osteocytes mimics skeletal aging. *J Biol Chem* **288**, 17432-17440, doi:10.1074/jbc.M112.444190 (2013).

56 Piemontese, M. *et al.* Low bone mass and changes in the osteocyte network in mice lacking autophagy in the osteoblast lineage. *Sci Rep* **6**, 24262, doi:10.1038/srep24262 (2016).

57 Shapiro, I. M., Layfield, R., Lotz, M., Settembre, C. & Whitehouse, C. Boning up on autophagy: the role of autophagy in skeletal biology. *Autophagy* **10**, 7-19, doi:10.4161/auto.26679 (2014).

58 Zahm, A. M., Bohensky, J., Adams, C. S., Shapiro, I. M. & Srinivas, V. Bone cell autophagy is regulated by environmental factors. *Cells Tissues Organs* **194**, 274-278, doi:10.1159/000324647 (2011).

59 Anderson, H. C. Molecular biology of matrix vesicles. *Clin Orthop Relat Res*, 266-280 (1995).

bioRxiv preprint doi: https://doi.org/10.1101/260711; this version posted February 5, 2018. The copyright holder for this preprint (which was not certified by peer review) is the author/funder. All rights reserved. No reuse allowed without permission.

60 Hoshi, K. & Ozawa, H. Matrix vesicle calcification in bones of adult rats. *Calcified tissue international* **66**, 430-434 (2000).

61 Rohde, M. & Mayer, H. Exocytotic process as a novel model for mineralization by osteoblasts in vitro and in vivo determined by electron microscopic analysis. *Calcified tissue international* **80**, 323-336, doi:10.1007/s00223-007-9013-5 (2007).

62 Mahamid, J. *et al.* Bone mineralization proceeds through intracellular calcium phosphate loaded vesicles: a cryo-electron microscopy study. *J Struct Biol* **174**, 527-535, doi:10.1016/j.jsb.2011.03.014 (2011).

63 Stanford, C. M., Jacobson, P. A., Eanes, E. D., Lembke, L. A. & Midura, R. J. Rapidly forming apatitic mineral in an osteoblastic cell line (UMR 106-01 BSP). *J Biol Chem* **270**, 9420-9428 (1995).

64 Qing, H. *et al.* Demonstration of osteocytic perilacunar/canalicular remodeling in mice during lactation. *J Bone Miner Res* **27**, 1018-1029, doi:10.1002/jbmr.1567 (2012).

65 Zambonin Zallone, A., Teti, A., Primavera, M. V. & Pace, G. Mature osteocytes behaviour in a repletion period: the occurrence of osteoplastic activity. *Basic Appl Histochem* **27**, 191-204 (1983).

66 Arthur, A., Koblar, S., Shi, S. & Gronthos, S. Eph/ephrinB mediate dental pulp stem cell mobilization and function. *Journal of dental research* **88**, 829-834, doi:10.1177/0022034509342363 (2009).

67 Heng, B. C. *et al.* EphrinB2 signaling enhances osteogenic/odontogenic differentiation of human dental pulp stem cells. *Arch Oral Biol* **87**, 62-71, doi:10.1016/j.archoralbio.2017.12.014 (2017).

68 Genet, F. *et al.* Neurological heterotopic ossification following spinal cord injury is triggered by macrophage-mediated inflammation in muscle. *J Pathol* **236**, 229-240, doi:10.1002/path.4519 (2015).

69 Mehrotra, R. Disordered mineral metabolism and vascular calcification in nondialyzed chronic kidney disease patients. *J Ren Nutr* **16**, 100-118, doi:10.1053/j.jrn.2006.01.006 (2006).

70 Yiu, A. J., Callaghan, D., Sultana, R. & Bandyopadhyay, B. C. Vascular Calcification and Stone Disease: A New Look towards the Mechanism. *J Cardiovasc Dev Dis* **2**, 141-164, doi:10.3390/jcdd2030141 (2015).

71 Spatz, J. M. *et al.* The Wnt Inhibitor Sclerostin Is Up-regulated by Mechanical Unloading in Osteocytes in Vitro. *Journal of Biological Chemistry* **290**, 16744-16758, doi:10.1074/jbc.M114.628313 (2015).

72 Gerety, S. S., Wang, H. U., Chen, Z. F. & Anderson, D. J. Symmetrical mutant phenotypes of the receptor EphB4 and its specific transmembrane ligand ephrin-B2 in cardiovascular development. *Molecular cell* **4**, 403-414 (1999).

73 Kalajzic, I. *et al.* Dentin matrix protein 1 expression during osteoblastic differentiation, generation of an osteocyte GFP-transgene. *Bone* **35**, 74-82, doi:10.1016/j.bone.2004.03.006

S8756328204001097 [pii] (2004).

bioRxiv preprint doi: https://doi.org/10.1101/260711; this version posted February 5, 2018. The copyright holder for this preprint (which was not certified by peer review) is the author/funder. All rights reserved. No reuse allowed without permission.

74 Johnson, R. W. *et al.* The primary function of gp130 signaling in osteoblasts is to maintain bone formation and strength, rather than promote osteoclast formation. *J Bone Miner Res* **29**, 1492-1505, doi:10.1002/jbmr.2159 (2014).

75 Chia, L. Y., Walsh, N. C., Martin, T. J. & Sims, N. A. Isolation and gene expression of haematopoietic-cell-free preparations of highly purified murine osteocytes. *Bone* **72**, 34-42, doi:10.1016/j.bone.2014.11.005 (2015).

76 Reddy, G. K. & Enwemeka, C. S. A simplified method for the analysis of hydroxyproline in biological tissues. *Clin Biochem* **29**, 225-229 (1996).

77 Liao, Y., Smyth, G. K. & Shi, W. The Subread aligner: fast, accurate and scalable read mapping by seed-and-vote. *Nucleic Acids Res* **41**, e108, doi:10.1093/nar/gkt214 (2013).

78 Phipson, B., Lee, S., Majewski, I. J., Alexander, W. S. & Smyth, G. K. Robust Hyperparameter Estimation Protects against Hypervariable Genes and Improves Power to Detect Differential Expression. *Ann Appl Stat* **10**, 946-963, doi:10.1214/16-AOAS920 (2016).

bioRxiv preprint doi: https://doi.org/10.1101/260711; this version posted February 5, 2018. The copyright holder for this preprint (which was not certified by peer review) is the author/funder. All rights reserved. No reuse allowed without permission.

Acknowledgements

The authors thank the staff of the St. Vincent's Health Bioresources Centre for excellent animal care and assistance. The authors also thank Mr Joshua Johnson for technical assistance with histology. Dr. Roger Curtain from Bio21 for technical assistance with BSEM, Dr. Paul Roschger for advice on BSEM analysis and Dr. Elefterios Paschalis for advice on collagen crosslinking analysis. This work was supported by NHMRC Grants 1042129 and 1081242 to NAS and TJM, Program Grant 1054618 to GKS, the Australian and New Zealand Bone and Mineral Society Christine and TJ Martin Travel Award to CV, and a Brockhoff Foundation Grant to CV. JSO was supported by an ARC Future Fellowship. NAS was supported by an NHMRC Senior Research Fellowship. St. Vincent's Institute acknowledges the support of the Victorian State Government OIS program. Part of this work was untaken at the Infrared Microspectroscopy Beamline at the Australian Synchrotron, part of ANSTO.

Author contributions

Conceptualization, C.V., T.J.M. and N.A.S.; Investigation, C.V., T.A.D., N.A., B.C.I., H.N., Y.H., M.I., G.K.S., N.A.S.; Data curation, C.V.; Analysis, C.V., T.A.D., N.A., C.P.; Writing – Original Draft, C.V., N.A.S.; Writing, Review & Editing, all authors; Visualization, C.V., N.A.S.; Supervision, N.A.S.; Project leadership, C.V., N.A.S.; Funding acquisition, N.A.S., T.J.M.

bioRxiv preprint doi: https://doi.org/10.1101/260711; this version posted February 5, 2018. The copyright holder for this preprint (which was not certified by peer review) is the author/funder. All rights reserved. No reuse allowed without permission.

Declaration of Interests

The authors declare no competing interests.

bioRxiv preprint doi: https://doi.org/10.1101/260711; this version posted February 5, 2018. The copyright holder for this preprint (which was not certified by peer review) is the author/funder. All rights reserved. No reuse allowed without permission.

Figure Legends

Figure 1: *Efnb2* is upregulated by PTH and PTHrP in osteocyte-like cells *in vitro* and confirmation of ephrinB2 knockdown *in vivo.* Ocy454 cells were differentiated on plastic plates for 14 days. Differentiated cells were treated with 10nM hPTH(1-34) or hPTHrP(1-141) for 6h; mRNA levels for *Efnb2* was measured by qRT-PCR (A). Data are mean ± SEM, n=6 replicates; representative of 3 independent experiments. shRNA knockdown of PTHrP (*Pthlh*) in Ocy454 cells were differentiated for 14 days on 3D scaffolds (B). Confirmation of knockdown of EphrinB2 (*Efnb2*) in osteocytes isolated from *Dmp1Cre.DMP1-GFP-Tg.Efnb2*$^{w/w}$ and *Dmp1Cre.DMP1-GFP-Tg.Efnb2*$^{f/f}$ mice (C). Data are represented as mean ± SEM of 2 experiments, n= 6 mice/group; pooled. *$p<0.05$, **$p<0.01$, ***$p<0.001$ compared to control by Student's t-test. B: N.D. = not detected.

Figure 2: 12-week-old female mice with EphrinB2 deficiency in osteocytes have impaired bone strength. A-F: Mechanical testing results: Average Load-Deformation curve (each dot represents the average load and deformation for the noted sample group; error bars were excluded to highlight the shape of curves) (A), Kaplan-Meier curve of percentage of unbroken femora ($p<0.0008$ based on Log-rank (Mantel-Cox) test) (B) and derived ultimate force (C), ultimate deformation (D), post-yield deformation (E) and energy absorbed to failure (F) taken from 3-point bending tests of *Dmp1Cre.Efnb2*$^{w/w}$ (w/w) and *Dmp1Cre.Efnb2*$^{f/f}$ (f/f) femora. Data

bioRxiv preprint doi: https://doi.org/10.1101/260711; this version posted February 5, 2018. The copyright holder for this preprint (which was not certified by peer review) is the author/funder. All rights reserved. No reuse allowed without permission.

are represented as mean ± SEM, n = 10-12/group. *p<0.05, **p<0.01, ***p<0.001 vs w/w controls.

Figure 3: Impaired strength in *Dmp1Cre.Efnb2$^{f/f}$* mice is a material defect. Femoral moment of inertia (A), Average stress-strain curve (each dot represents the average load and deformation for the noted sample group; error bars were excluded to highlight the shape of curves) (B), ultimate stress (C), ultimate strain (D), toughness (E) derived from 3-point bending tests of 12-week old female *Dmp1Cre.Efnb2$^{w/w}$* (w/w) and *Dmp1Cre.Efnb2$^{f/f}$* (f/f) femora. Indentation distance increased derived from reference point indentation of femora (F). Data are represented as mean ± SEM, n = 10-12/group. *p<0.05, **p<0.01 vs w/w controls.

Figure 4: No defect in cortical tissue mineral density or periosteal bone formation in *Dmp1Cre.Efnb2$^{f/f}$* mice. A-C: Cortical data: Cortical thickness (A), Periosteal perimeter (B), Marrow area (C), Cortical tissue mineral density (TMD) (D), periosteal mineralizing surface (Ps.MS/BS) (E) and periosteal mineral appositional rate (Ps.MAR) (F). Data are represented as mean ± SEM, n = 10-12/group (microCT), 7-11/group (histomorphometry).

Figure 5: Elevated mineral accrual and carbonate deposition in 12-week old female *Dmp1Cre.Efnb2$^{f/f}$* periosteum. A: Regions of periosteal bone used for sFTIRM analysis, regions 1-3 (15μm^2 in size) denote bone areas of increasing maturity. B: Average FTIR spectra of *Dmp1Cre.Efnb2$^{w/w}$* (w/w) and *Dmp1Cre.Efnb2$^{f/f}$* (f/f) tibiae collected from region 2. C-E: sFTIRM-derived mineral:matrix (C), carbonate:mineral (D) and amide I:II (E) ratios in regions 1-3 of w/w and f/f tibiae.

bioRxiv preprint doi: https://doi.org/10.1101/260711; this version posted February 5, 2018. The copyright holder for this preprint (which was not certified by peer review) is the author/funder. All rights reserved. No reuse allowed without permission.

Data are represented as mean ± SEM, n = 13/group. *p<0.05, **p<0.01, ***p<0.001 vs region 1 of same genotype (bone maturation effect), $^{+}$p<0.05, $^{++}$p<0.01 vs w/w in the same region (genotype effect).

Figure 6: Polarized FTIR imaging confirms altered collagen distribution in 12-week old female *Dmp1Cre.Efnb2$^{f/f}$* mice. Representative FTIR images of the cortical midshaft from *Dmp1Cre.Efnb2$^{w/w}$* and *Dmp1Cre.Efnb2$^{f/f}$* mice under the (A,B) 0° and (D,E) 90° polarizing filters. Quantification of the amide I:II ratio under the (C) 0° and (F) 90° polarizing filter in periosteal, intracortical and endocortical regions. Data are represented as mean ± SEM, n = 12-13/group. *p<0.05 vs *Dmp1Cre.Efnb2$^{w/w}$* of same region, +p<0.05, ++p<0.01, +++p<0.001 vs same genotype between different regions.

Figure 7. RNA sequencing from marrow-flushed femora of 12-week old female *Dmp1Cre.Efnb2$^{f/f}$* mice show upregulation of autophagy-related genes, compared to controls. Up-regulated (A) and down-regulated (B) genes from RNA of *Dmp1Cre.Efnb2$^{f/f}$* mice compared to controls; genes associated with autophagy are indicated by *. Columns give Entrez Gene ID, log2-fold-change, average log2-expression, moderated t-statistic, P-value and false discovery rate (FDR). *Efnb2* knockdown confirmed in Ocy454 cells differentiated for 7, 11 and 14 days (C) and fold change of LC3-II:I ratio in *Efnb2* shRNA knockdown cells treated with chloroquine (CQ) for 4 hours compared to basal levels of each construct. Data are represented as mean ± SEM, n = 3 technical replicates, *p<0.05 vs. vector control.

Figure 8. Model of how osteocytic ephrinB2 regulates bone matrix composition. (A) In control bone (*Dmp1Cre.Efnb2$^{w/w}$*) both osteoblasts and

bioRxiv preprint doi: https://doi.org/10.1101/260711; this version posted February 5, 2018. The copyright holder for this preprint (which was not certified by peer review) is the author/funder. All rights reserved. No reuse allowed without permission.

osteocytes express ephrinB2. Osteoblasts reside on the bone surface and pass through a transition (dashed arrows) to become mature, matrix embedded osteocytes. The process of bone matrix maturation is shown on the right of each panel, with the three measurement regions (1, 2, 3). Osteoblasts deposit collagen-containing osteoid (triple helical collagen fibers). In the first region of newly-formed bone, mineral deposition is initiated. Mineral crystals (yellow stars) and carbonate (orange circles) continue to accumulate, and collagen fibers become more compact as the matrix matures. (B) *Dmp1Cre.Efnb2*$^{f/f}$ mice express ephrinB2 in osteoblasts, but not osteocytes. The transition of osteoblasts to osteocytes is increased resulting in increased osteocyte density, and osteocytes have increased levels of autophagic flux (green cells). Osteoid deposition occurs normally, and the initiation of mineralization commences at the same rate (red arrow), but as soon as it starts, mineral deposition occurs at a greater level in newly-formed bone (region 1) and in more mature bone regions (2, and 3) to reach a level where there is more mineral, more carbonate substitution and more compaction of collagen fibers compared to controls. Ultimately this leads to more brittle bone.

bioRxiv preprint doi: https://doi.org/10.1101/260711; this version posted February 5, 2018. The copyright holder for this preprint (which was not certified by peer review) is the author/funder. All rights reserved. No reuse allowed without permission.

Table 1. Additional structural and material properties determined by microCT and 3-point bending tests in 12-week old female *Dmp1Cre.Efnb2*$^{f/f}$ femora, compared to controls.

	Dmp1Cre.Efnb2 $^{w/w}$	***Dmp1Cre.Efnb2*** $^{f/f}$
Structural properties		
Yield Force (N)	14.98 ± 0.63	11.15 ± 0.90[b]
Yield deformation (mm)	0.18 ± 0.01	0.12 ± 0.01[b]
Stiffness (N/mm)	139.32 ± 10.16	134.59 ± 10.31
Anteroposterior (AP) width (mm)	1.24 ± 0.02	1.25 ± 0.02
Mediolateral (ML) width (mm)	1.80 ± 0.03	1.75 ± 0.01
Material properties		
Yield Stress (MPa)	31.96 ± 2.12	24.15 ± 1.81[a]
Yield Strain (%)	0.04 ± 0.002	0.02 ± 0.001[b]
Elastic Modulus (MPa)	1430.45 ± 105.75	1320.44 ± 93.45

Data are represented as mean ± SEM; n = 12/group

[a]$p < 0.05$ versus *Dmp1Cre.Efnb2* $^{w/w}$ controls, Student's t-test.

[b]$p < 0.01$ versus *Dmp1Cre.Efnb2* $^{w/w}$ controls, Student's t-test.

Table 2. Histomorphometric analyses of tibial trabecular bone in 12-week old female *Dmp1Cre.Efnb2*$^{f/f}$ femora, compared to controls.

	Dmp1Cre.Efnb2 $^{w/w}$	***Dmp1Cre.Efnb2*** $^{f/f}$
Mineral apposition rate (µm/day)	2.09 ± 0.09	1.96 ± 0.10
Mineralizing surface/Bone surface (%)	34.51 ± 2.52	34.87 ± 1.04
Bone Formation Rate/Bone Surface ($\mu m^2/\mu m$/day)	0.71 ± 0.04	0.68 ± 0.04
Osteoid Thickness (µm)	2.26 ± 0.17	2.66 ± 0.21
Osteoid Surface (%)	7.39 ± 1.45	9.83 ± 2.29
Osteoblast Surface (%)	13.60 ± 1.81	16.25 ± 2.20

bioRxiv preprint doi: https://doi.org/10.1101/260711; this version posted February 5, 2018. The copyright holder for this preprint (which was not certified by peer review) is the author/funder. All rights reserved. No reuse allowed without permission.

Osteoclast Surface (%)	8.78 ± 1.25	11.58 ± 0.95

Data are represented as mean ± SEM; n = 7-11/group

Table 3. Collagen fiber deposition and osteocyte lacunae parameters in the femoral midshaft from 12-week old female *Dmp1Cre.Efnb2*$^{w/w}$ (w/w) and *Dmp1Cre.Efnb2*$^{f/f}$ (f/f) mice by polarized light microscopy and backscattered electron microscopy.

	***Dmp1Cre.Efnb2*$^{w/w}$**	***Dmp1Cre.Efnb2*$^{f/f}$**
Woven bone (%)	17.00 ± 1.58	19.33 ± 2.30
Hydroxyproline (µg/mg of protein)	36.38 ± 3.37	44.51 ± 2.87[a]
Osteocyte lacunar size (µm²)	35.27 ± 1.09	35.76 ± 0.83
Osteocyte lacunar size of the largest 20% (µm²)	59.81 ± 2.05	60.11 ± 2.05
Osteocyte lacunar density (/mm²)	232.91 ± 12.27	268.75 ± 9.26[a]

Data are represented as mean ± SEM; n = 10-12/group

[a]$p < 0.05$ versus *Dmp1Cre.Efnb2* $^{w/w}$ controls, Student's t-test.

Figure 1

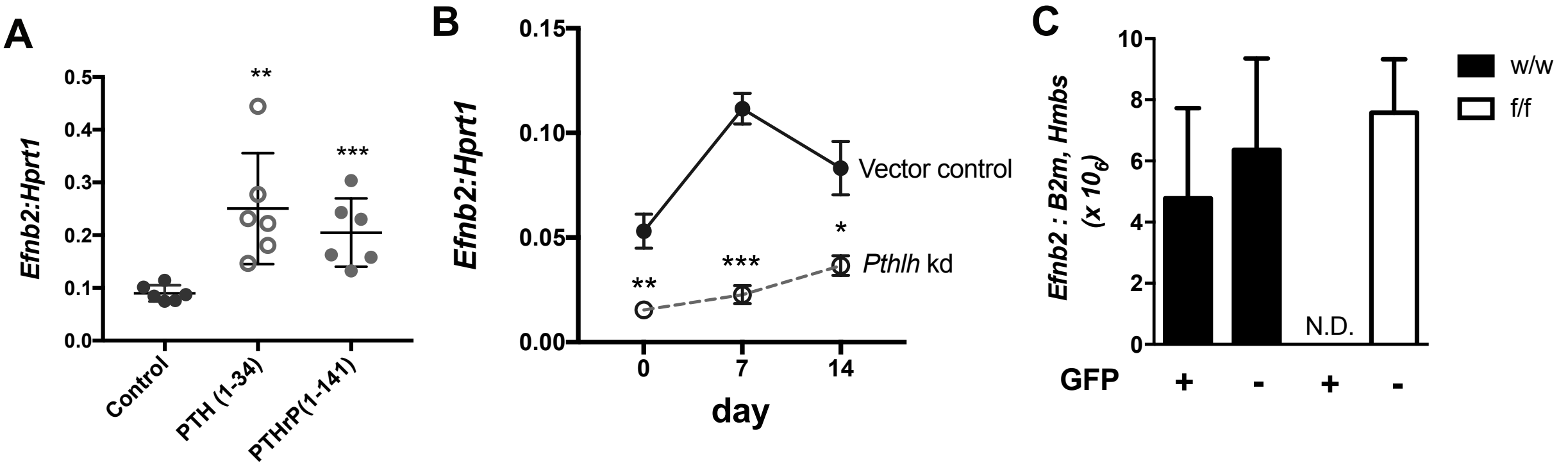
A
Efnb2:Hprt1
0.5
0.4
0.3
0.2
0.1
0.0
**
***
Control
PTH (1-34)
PTHrP(1-141)
B
Efnb2:Hprt1
0.15
0.10
0.05
0.00
Vector control
Pthlh kd
**
***
*
0
7
14
day
C
Efnb2 : B2m, Hmbs
(x 10^6)
10
8
6
4
2
0
w/w
f/f
N.D.
GFP
+
-
+
-

Figure 2

bioRxiv preprint doi: https://doi.org/10.1101/260711; this version posted February 5, 2018. The copyright holder for this preprint (which was not certified by peer review) is the author/funder. All rights reserved. No reuse allowed without permission.

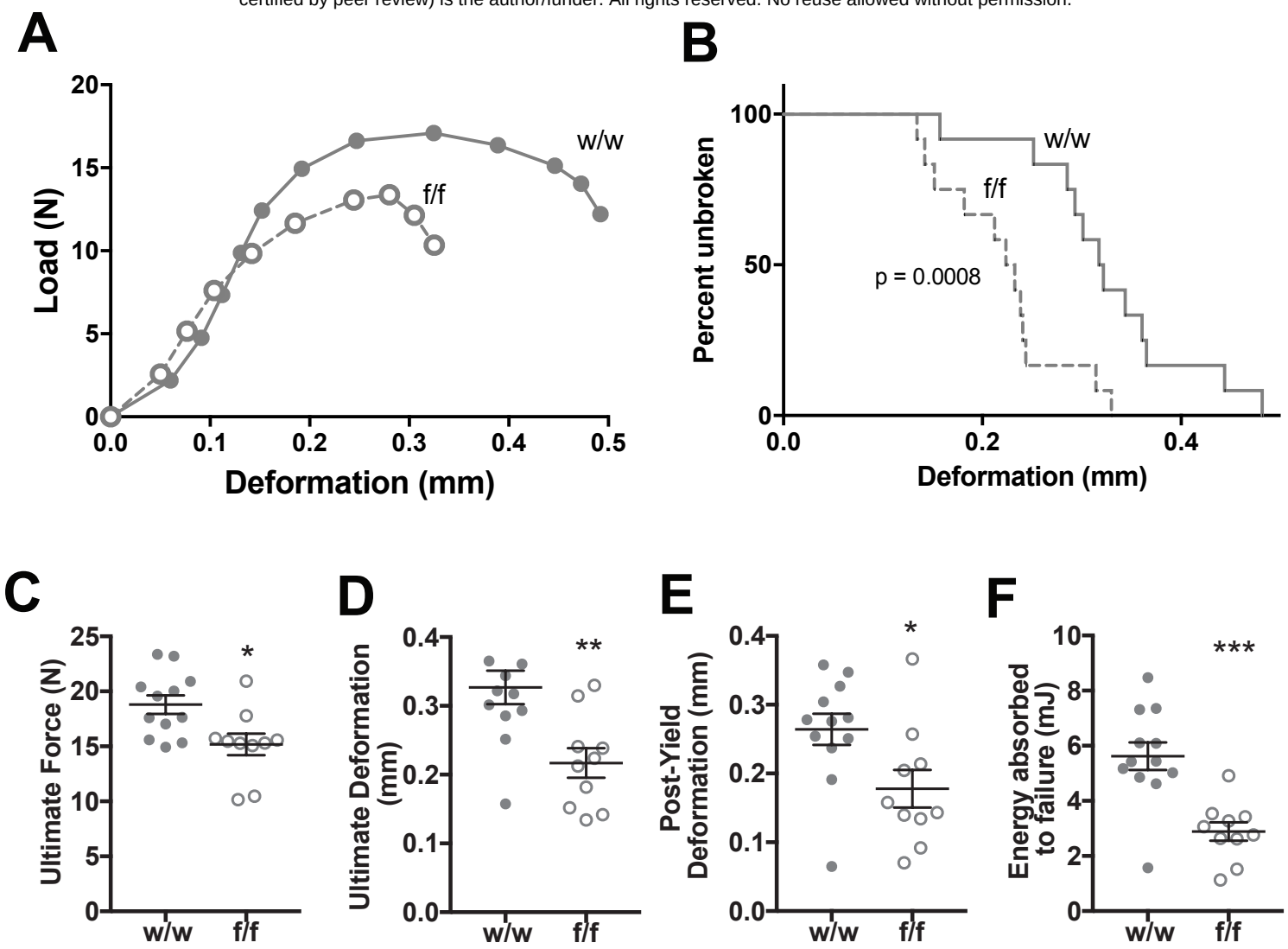

Figure 3

bioRxiv preprint doi: https://doi.org/10.1101/260711; this version posted February 5, 2018. The copyright holder for this preprint (which was not certified by peer review) is the author/funder. All rights reserved. No reuse allowed without permission.

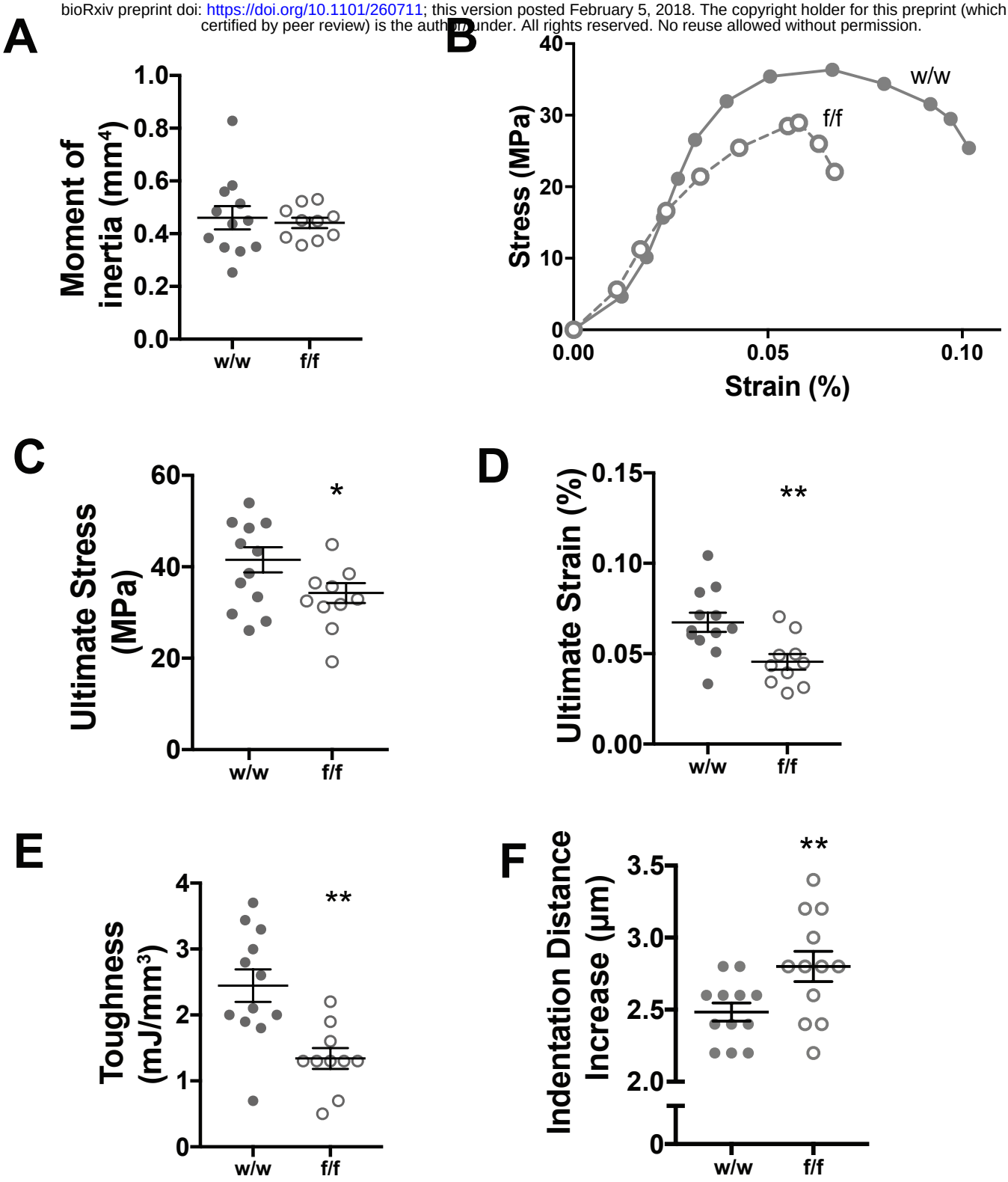

Figure 4

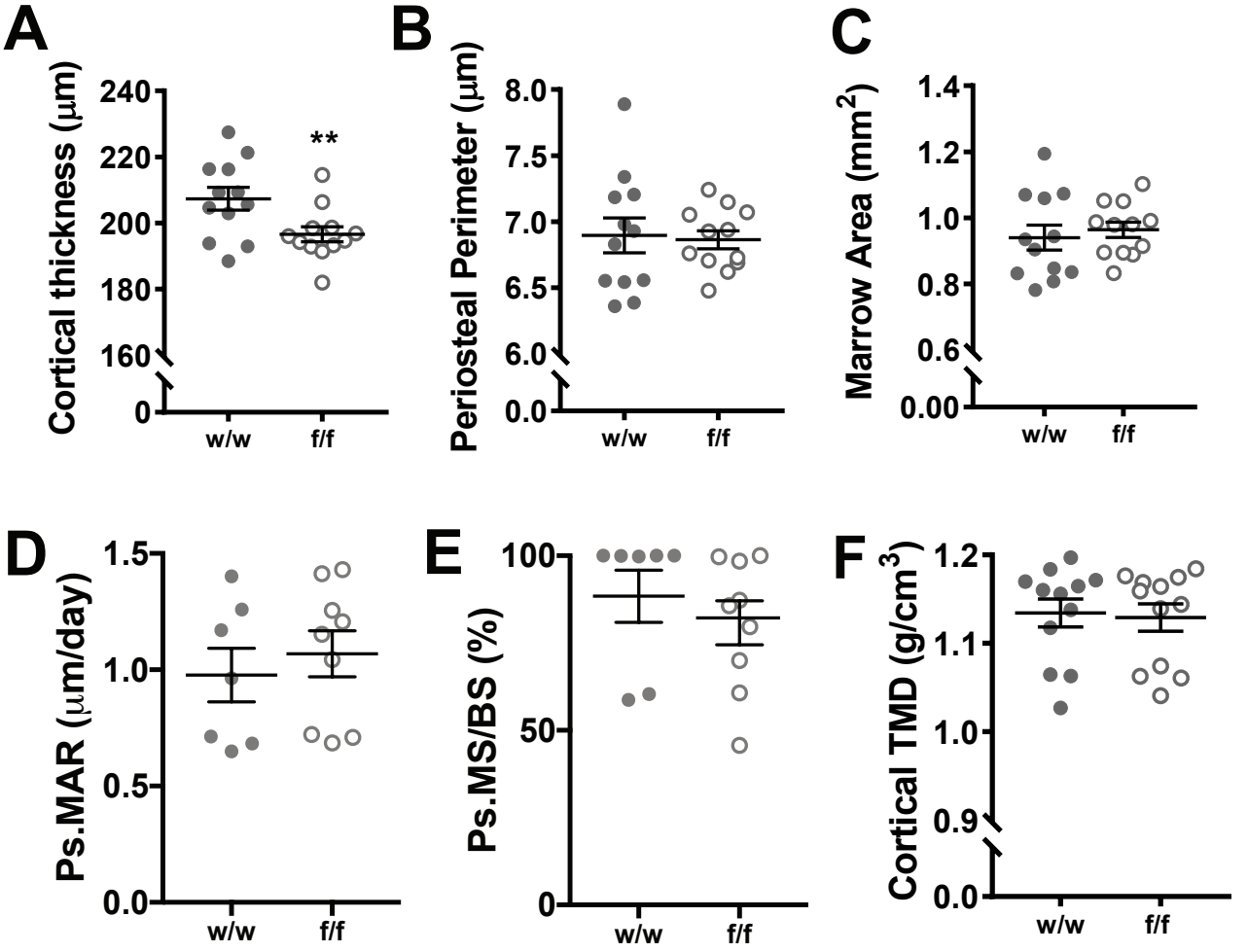
A
Cortical thickness (μm)
240
220
200
180
160
0
**
w/w
f/f
B
Periosteal Perimeter (μm)
8.0
7.5
7.0
6.5
6.0
0.0
w/w
f/f
C
Marrow Area (mm2)
1.4
1.2
1.0
0.8
0.6
0.00
w/w
f/f
D
Ps.MAR (μm/day)
1.5
1.0
0.5
0.0
w/w
f/f
E
Ps.MS/BS (%)
100
50
0
w/w
f/f
F
Cortical TMD (g/cm3)
1.2
1.1
1.0
0.9
0.0
w/w
f/f

Figure 5

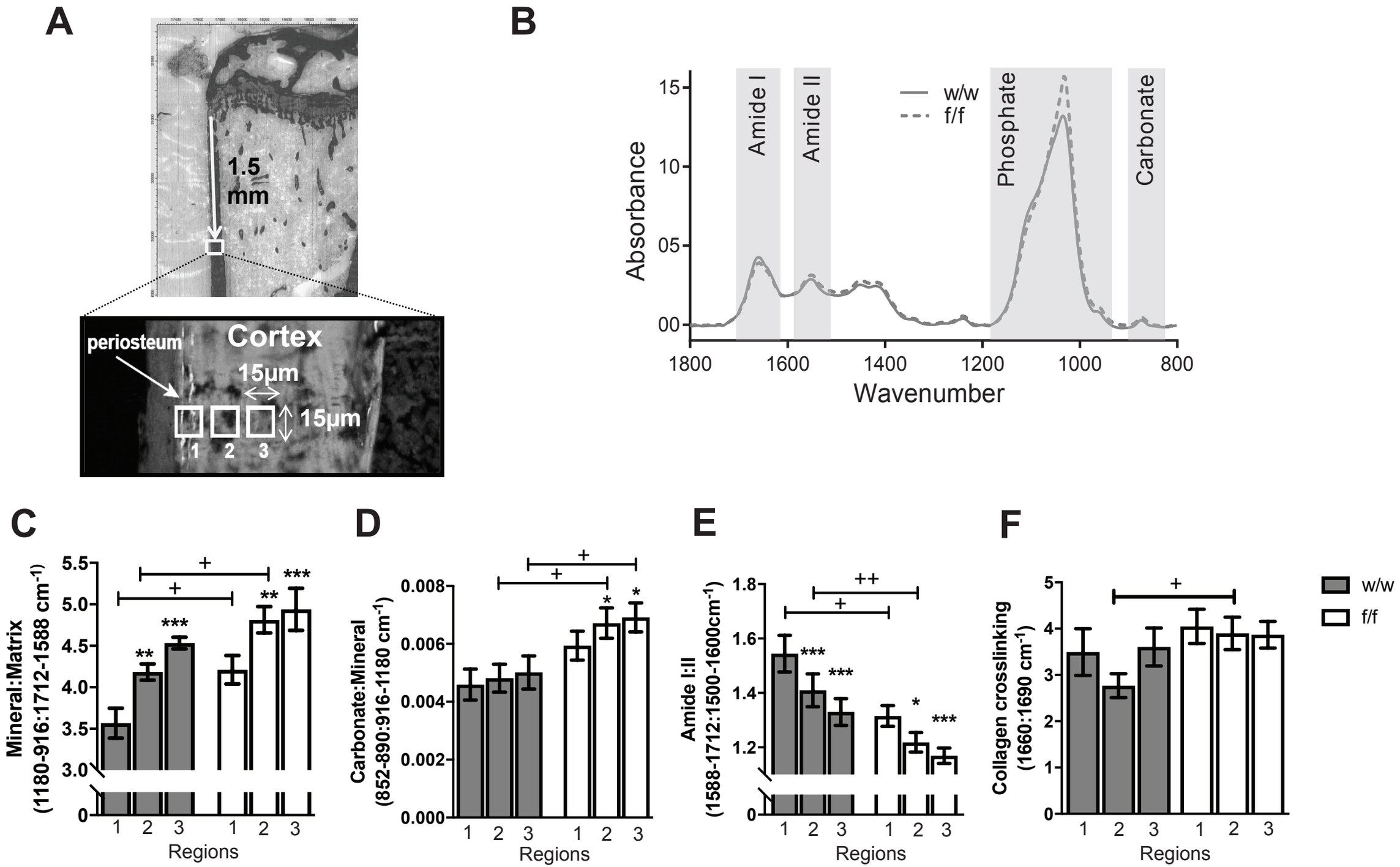
A
1.5 mm
periosteum
Cortex
15µm
15µm
1 2 3
B
Amide I
Amide II
Phosphate
Carbonate
w/w
f/f
Absorbance
Wavenumber
C
Mineral:Matrix (1180-916:1712-1588 cm-1)
Regions
D
Carbonate:Mineral (852-890:916-1180 cm-1)
Regions
E
Amide I:II (1588-1712:1500-1600cm-1)
Regions
F
Collagen crosslinking (1660:1690 cm-1)
Regions
w/w
f/f

certified by peer review) is the author/funder. All rights reserved. No reuse allowed without permission.

Figure 6

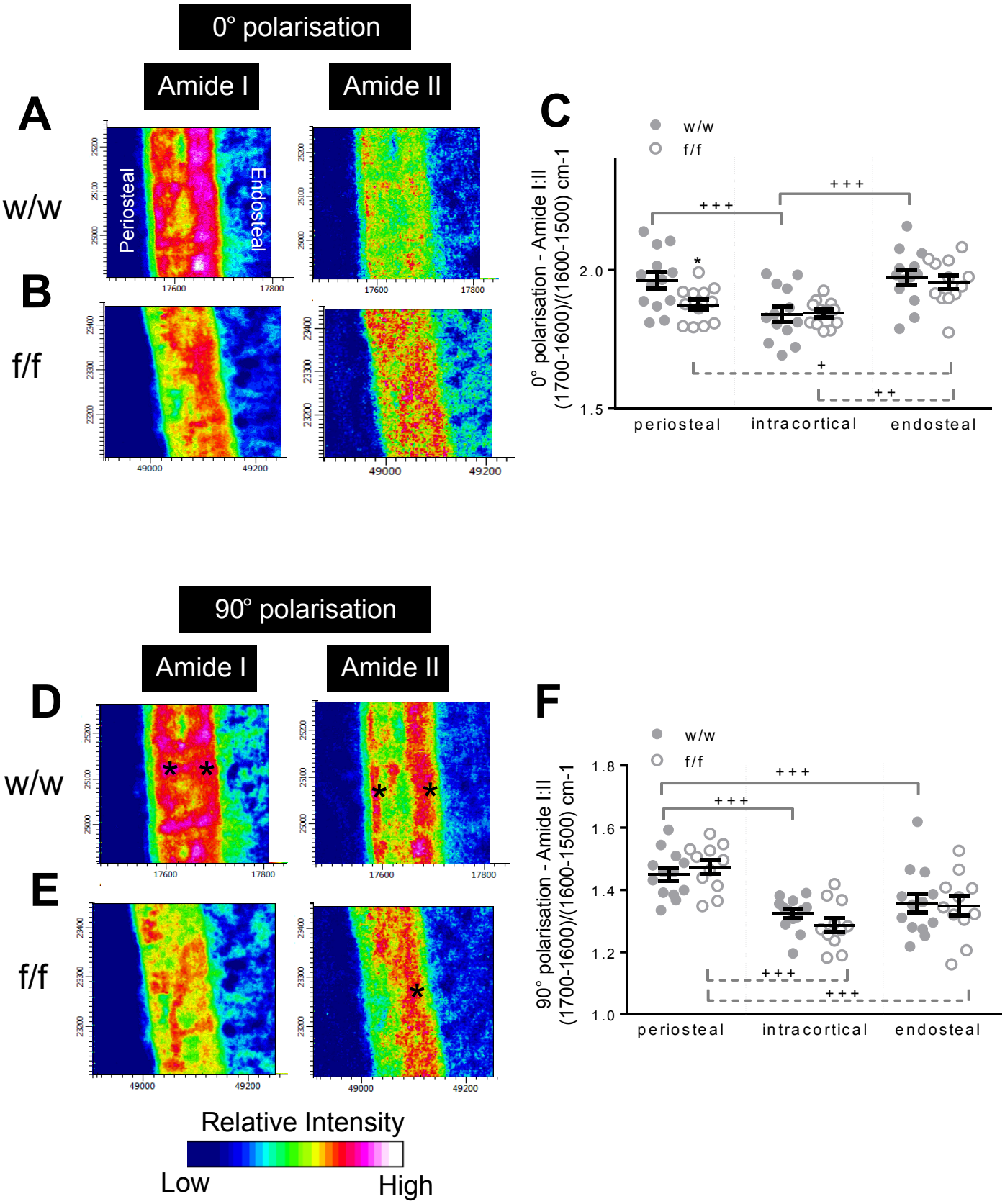

Figure 7

bioRxiv preprint doi: https://doi.org/10.1101/260711 this version posted February 5, 2018. The copyright holder for this preprint (which was not ... permission.

A

Gene	Gene ID	Log2FC	Average Expression	T	P-value	FDR
Pira6	18729	1.788	2.245	10.52	3.19E-06	0.009485
Fam134b *	66270	1.907	6.821	10.51	3.22E-06	0.009485
Fbxo32 *	67731	2.443	7.223	10.33	3.71E-06	0.009485
Vldlr	22359	1.224	6.325	10.3	3.80E-06	0.009485
Abca8a	217258	1.116	5.984	9.99	4.84E-06	0.009761
Cnksr1	194231	1.246	3.741	9.71	6.07E-06	0.009761
Lama2 *	16773	1.475	6.078	9.37	8.05E-06	0.009761
Bnip3 *	12176	1.363	5.117	9.21	9.31E-06	0.009761
Slc7a2	11988	1.437	5.507	9.19	9.46E-06	0.009761
Trim63 *	433766	2.476	7.151	9.02	1.09E-05	0.010188
Cped1	214642	0.993	5.745	8.92	1.19E-05	0.010288
Klf9	16601	0.816	6.472	8.77	1.37E-05	0.010288
Zim1	22776	1.597	1.624	8.55	1.66E-05	0.010288
Peg3 *	18616	1.748	4.988	8.44	1.84E-05	0.010288
Abca6	76184	1.576	3.62	8.44	1.84E-05	0.010288
Slc15a2	57738	1.446	4.194	8.43	1.86E-05	0.010288
Myo15	17910	1.291	2.933	8.09	2.56E-05	0.011489

B

Gene	Gene ID	Log2FC	Average Expression	T	P-value	FDR
Ccdc92b	432582	-3.679	2.509	-17.73	4.23E-08	0.000634
BC049730	232972	-5.568	2.26	-11.2	1.92E-06	0.009485
Sec14l2	67815	-1.066	5.35	-9.69	6.20E-06	0.009761
2610507I01Rik	72203	-4.421	3.956	-9.56	6.88E-06	0.009761
Eps8l1 *	67425	-4.1	2.602	-9.47	7.41E-06	0.009761
Pirb	18733	-1.242	6.794	-9.15	9.78E-06	0.009761
Fam110c	104943	-3.115	0.935	-8.87	1.25E-05	0.010288
Klf1 *	16596	-1.095	7.14	-8.7	1.45E-05	0.010288
Abcg4	192663	-0.884	5.372	-8.49	1.76E-05	0.010288
Tspo2 *	70026	-1.1	5.864	-8.46	1.80E-05	0.010288
Unc5a *	107448	-1.321	3.183	-8.45	1.83E-05	0.010288
Sycp1	20957	-3.876	-0.345	-8.17	2.37E-05	0.011489
Unc5cl	76589	-1.527	2.332	-8.16	2.40E-05	0.011489

C

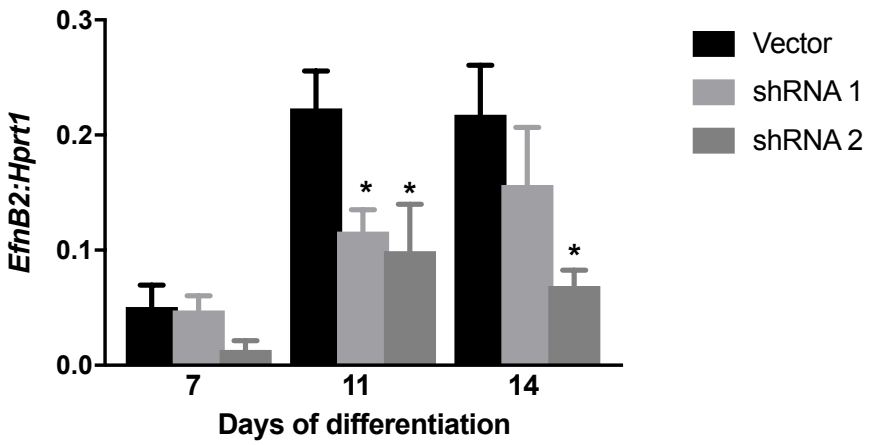

D

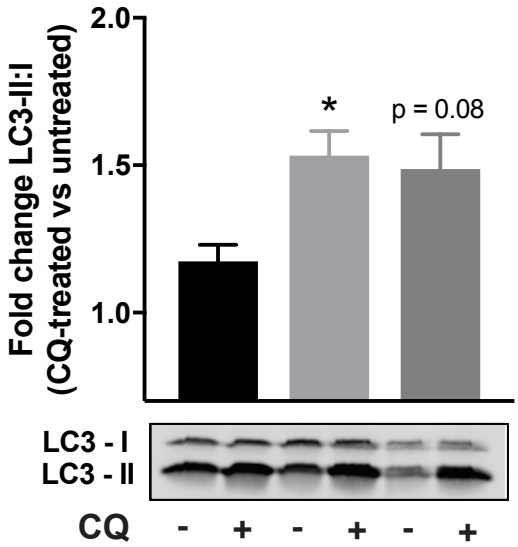

Figure 8

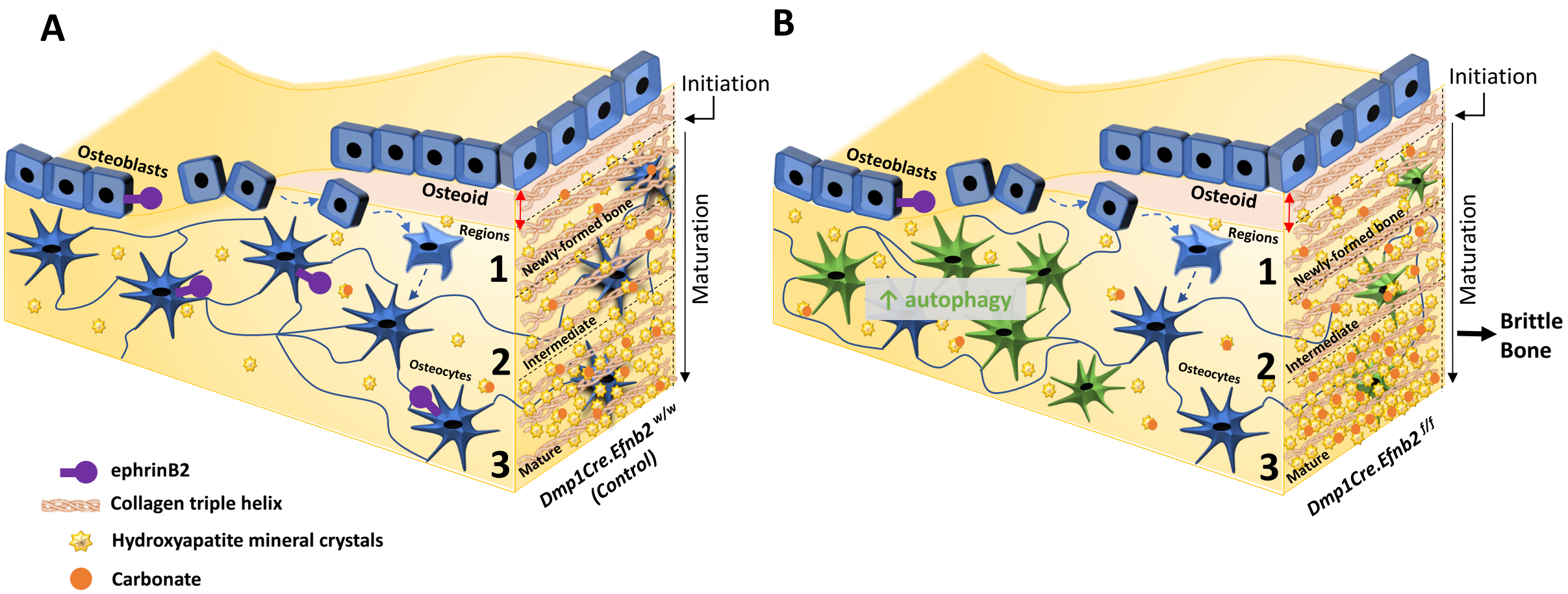
A
Osteoblasts
Osteoid
Regions
1
2
3
Osteocytes
Newly-formed bone
Intermediate
Mature
Initiation
Maturation
Dmp1Cre.Efnb2 w/w
(Control)
ephrinB2
Collagen triple helix
Hydroxyapatite mineral crystals
Carbonate
B
Osteoblasts
Osteoid
Regions
1
2
3
Osteocytes
↑ autophagy
Newly-formed bone
Intermediate
Mature
Initiation
Maturation
Brittle
Bone
Dmp1Cre.Efnb2 f/f